POLITECNICO
MILANO 1863

SCUOLA DI INGEGNERIA INDUSTRIALE
E DELL'INFORMAZIONE

A critical assessment on the mechanical load severity comparison, with focus on aerospace applications

Tesi di Laurea Magistrale in
Space Engineering - Ingegneria Spaziale

Author: **Fabio Cavagna**

Student ID: 996853
Advisor: Prof. Lorenzo Dozio
Co-advisor: Dr. Pietro Nali
Academic Year: 2022-23

Abstract

In the operational lifecycle of diverse items, ranging from consumer electronics to advanced aerospace components like aircraft and satellites, the ability to withstand various environmental conditions and mechanical stresses is paramount. Therefore, during the design and development phases of those items, proactive measures such as qualification testing are taken to ensure the resilience and survivability of the items when faced with challenges during their lifecycle. However, challenges arise when qualification loads differ significantly from real-world operative loads, necessitating a robust metric to assess load severity.

This is a collaborative thesis between Politecnico di Milano and Thales Alenia Space. It addresses two primary objectives. Firstly, it undertakes a comprehensive evaluation of existing methodologies employed to assess and compare load severities, which all applies to Single Degree of Freedom (SDOF) system loads. These methodologies are scrutinized for accuracy, computational efficiency, and potential for enhancement. Secondly, it introduces a convenient approach for load severity comparison. This proposed methodology transcends traditional techniques based on SDOF systems' absolute acceleration and focuses instead on analyzing interface forces in response to a 6 Degree of Freedom (6DOF) load.

Through this research, some insights are offered in order to assess and clarify the role of a number of techniques used to quantify the mechanical load severity. The study highlights the limitations of current severity assessment methods, particularly in complex systems, justifying the need for more accurate approaches. The methodology proposed in this work aims at enabling to perform the mechanical load severity comparison in case of Multi Degree of Freedom (MDOF) loading. The latter MDOF loading severity comparison corresponds to a specific need in the aerospace field, where MDOF shakers are entering the market for the qualification testing of space structures.

Keywords: Mechanical Load Severity Comparison, MDOF base excitations, 6DOF shakers, 6DOF transient loading

Abstract in lingua italiana

Nel ciclo operativo di diversi oggetti, che vanno dall'elettronica di consumo a componenti aerospaziali avanzati come aeromobili e satelliti, la capacità di resistere a varie condizioni ambientali e sollecitazioni meccaniche è fondamentale. Pertanto, durante le fasi di progettazione e sviluppo di tali oggetti, si adottano misure proattive come i test di qualificazione per garantire la resilienza e la sopravvivenza degli oggetti quando devono affrontare sfide nel corso del loro ciclo di vita. Tuttavia, emergono delle sfide quando i carichi di qualificazione differiscono in modo significativo dai carichi operativi del mondo reale, rendendo necessaria una metrica robusta per valutare la gravità del carico.

Questa è una tesi collaborativa tra il Politecnico di Milano e Thales Alenia Space. Affronta due obiettivi principali. In primo luogo, si effettua una valutazione delle metodologie esistenti impiegate per valutare e confrontare le severità dei carichi, tutte applicabili a sistemi a 1 Grado di Libertà (1GDL). Queste metodologie vengono esaminate per accuratezza, efficienza computazionale e potenziale per miglioramenti. In secondo luogo, si introduce una metodologia conveniente per il confronto della severità di un carico definito in più Gradi di Libertà (GDL). Nello specifico, il metodo proposto supera le tecniche tradizionali basate sull'accelerazione assoluta dei sistemi a 1GDL e si concentra invece sull'analisi delle forze di interfaccia in risposta a un carico a 6 Gradi di Libertà (6GDL).

Attraverso questa ricerca, si offrono informazioni e metodologie per migliorare la valutazione della severità dei carichi. Questo sforzo rafforza alla fine l'affidabilità e la robustezza degli oggetti in una vasta gamma di applicazioni. Lo studio evidenzia i limiti dei metodi attuali di valutazione della severità, in particolare nei sistemi complessi, giustificando la necessità di approcci più precisi. La metodologia proposta in questo lavoro mira a consentire il confronto della gravità dei carichi meccanici in caso di carichi a Molti Gradi di Libertà (MGDL). Quest'ultimo confronto della gravità dei carichi MGDL corrisponde a una specifica esigenza nel campo aerospaziale, dove i sistemi di eccitazione MGDL stanno entrando nel mercato per i test di qualificazione delle strutture spaziali.

Parole chiave: Confronto gravità carichi meccanici, Eccitazione di base MGDL, Vibratori a 6GDL, Transitori a 6GDL

Contents

1 | Introduction

1.1. Motivation of the work

In the course of their operational lifespan, everyday items, ranging from mobile phones and computers to wristwatches, cars, and even advanced aerospace components like aircraft and satellites, are subjected to an array of environmental conditions. These conditions encompass temperature fluctuations, humidity variations, and mechanical stresses. Therefore, it is of paramount importance, during the design and development phases of these items, to take proactive measures to ensure their resilience and survivability when faced with the diverse challenges they may encounter over their lifecycle. One such crucial measure is qualification testing.

Qualification testing serves as a pivotal step in the development process, verifying that an item can endure and thrive in the anticipated operating conditions. However, certain scenarios arise where the qualification load differs significantly from the operative load that the item will experience in real-world use. This is where the concept of "severity" comes into play, serving as a metric to quantitatively assess and compare the risk of failure when subjected to various loads. In simpler terms, if the severity of load A surpasses that of a different load B, it implies that the risk of failure for the item under load A is higher. In the context of testing, it's essential that the severity of the qualification load exceeds that of the operative load to ensure robustness.

This thesis, conducted in collaboration with *Thales Alenia Space*, focuses on two primary objectives:

1. **Evaluation and Enhancement of Current Methodologies**: The first objective revolves around a comprehensive investigation of existing methodologies employed for evaluating and comparing the severities of different mechanical loads. This entails scrutinizing their accuracy, computational efficiency, and any possible areas for improvement.

2. **Alternative Approach for Load Severity Comparison**: The second objective

involves proposing an innovative approach for comparing the severity of Multi Degree of Freedom (MDOF) mechanical loads. Unlike traditional methods that rely on the absolute acceleration of a Single Degree of Freedom (SDOF) system, this novel approach hinges on analyzing the interface (IF) forces acting on a system subjected to a 6 Degree of Freedom (6DOF) load.

Through the pursuit of these objectives, this research aims to contribute valuable insights and methodologies to enhance the assessment of load severities, ultimately bolstering the reliability and robustness of items across a spectrum of applications.

1.2. Literature review

Mechanical shocks and vibrations are pervasive in numerous engineering domains, including aerospace, naval, and defense engineering. Their capacity to jeopardize the structural integrity of systems has spurred a substantial body of research in this field. The literature pertinent to this thesis encompasses classical methodologies for assessing the severity of mechanical loads, including Shock Response Spectrum (SRS), Extreme Response Spectrum (ERS), and Fatigue Damage Spectrum (FDS). It delves into their practical applications, explores avenues for enhancing existing methodologies, and also delves into contemporary research on multiaxial shakers.

1.2.1. SRS

The concept of SRS was first introduced by Biot in 1932 [9]. Several techniques have been employed to evaluate the SRS. Craig [10] proposed numerical evaluation methods using recursive formulas, which utilize second-order integration techniques to approximate the excitation of a SDOF system through piecewise-constant or piecewise-linear interpolation. Additionally, an average acceleration method has been suggested as an alternative approach for determining the response of both linear and nonlinear systems. This method involves approximating the derivatives appearing in the system equation of motion and generating a step-by-step solution using time steps. However, these formulas were not easily solvable using calculators, leading to the development of recursive filtering techniques by Kelly-Richman [20]. Smallwood [29] further improved upon these techniques, providing more accurate results at higher natural frequencies.

1.2.2. ERS

Lalanne extensively studied the ERS [22]. His research started from analyzing the statistical properties of random vibrations in the time domain and the statistics of extreme values. Lalanne established relationships that define the response of a SDOF linear system to random vibrations, thus providing a clear definition of ERS. While the value of a random vibration sample provides an overall understanding of the vibration's severity, it is essential to determine the continuous frequency spectrum of the vibration to comprehend its effects on a structure. This frequency analysis is performed using the Power Spectral Density (PSD), which is an ideal tool for describing random vibrations. Knowledge of the PSD alone allows for accessing the distribution of maxima in a random signal without having to count individual peaks. This information is useful for pre-sizing structures. Furthermore, the PSD is used to determine the response of a SDOF system, which is necessary for calculating the Extreme Response of the given vibration.

1.2.3. FDS

Several studies indicate a relationship between stress, fatigue, and pseudo velocity (PV). Gaberson [14] and Hunt [17] consider the stress mechanisms of longitudinal waves in rods and transverse waves in beams, demonstrating that modal stress is only a function of velocity and independent of frequency. However, when evaluating the FDS, stress related to acceleration, as proposed by DiMaggio [12], and stress related to relative displacement, as highlighted by Lalanne [23], are also taken into consideration. DiMaggio [12] proposed a damage-based approach as an alternative to the traditional maximax analysis of nonstationary flight data for space and launch vehicles (LVs). This approach avoids overestimating peak response and addresses the potential for fatigue failure of hardware. The method employs an extended response spectrum analysis and includes amplitude-cycle counts, resulting in a conservative, stationary test specification that envelopes the damage potential of the nonstationary flight environment for both peak response and fatigue. McNeill [24] discusses the evaluation of the FDS in both the time and frequency domains, considering stress proportional to PV. His work shows that the two curves are equivalent. McNeill also explores the concept of Fatigue Damage Equivalent Testing (FDET), which utilizes the FDS as a measure of environment severity. FDET involves deriving a Gaussian random test environment and duration that is fatigue equivalent to a non-stationary environment described by an acceleration time history. The time history is typically obtained through direct measurement of the environment. The purpose of McNeill's paper is to provide a unified theoretical framework for the FDS and FDET, introducing im-

provements such as accounting for the PSD shape in the computation of the FDS in the frequency domain and estimating the overall test duration in the FDET.

1.2.4. Practical use of the severity

Lalanne [23] addresses the use of severity and response spectrum to develop specification, covering the ERS and FDS for sinusoidal and random vibrations. The extreme response and fatigue damage spectra are defined for each type of stress, including sinusoidal vibrations, swept sine, shocks, and random vibrations. The process of establishing a specification based on the equipment's lifecycle profile is detailed, taking into account the uncertainty factor, which involves uncertainties related to the dispersion of the real environment and the mechanical strength. Additionally, the test factor, which depends on the number of tests performed to demonstrate the equipment's resistance, is considered.

1.2.5. Improvements in the methods

When evaluating ERS and FDS, the input to the SDOF system is a PSD, and the output is the root mean square of a quantity such as acceleration, PV, or relative displacement. The methods mentioned above integrate the square of the transmissibility multiplied by the input PSD and take the square root to evaluate the root mean square. An alternative method is the use of Lyapunov equations, which involve creating a shape filter and connecting it to the SDOF system, as demonstrated by Wijker [31]. This alternative approach could enhance the efficiency of numerical codes.

In [19], Tom Irvine utilized FDS to compare the effects of different PSD specification, taking into account the varying durations of the specification. However, this comparison focused on stress related to acceleration and did not explore whether similar results could be achieved using a different approach. A comparison between two approaches, stress related to acceleration and stress related to PV, can be found in [15], where Grillo reviewed the approaches proposed by DiMaggio [12] and McNeill [24] for synthesizing equivalent random vibration test specification. The results obtained using both methods were quite similar, suggesting that the choice of approach may not significantly impact the outcomes of a comparison between different PSD specification.

1.2.6. Multiaxial shakers

Multiaxial shakers made their debut in the automotive industry during the early 1970s, as documented by Dodds [13]. Their utility then expanded to include the simulation of

seismic loads induced by earthquakes [21]. However, the aerospace sector has been somewhat slower to embrace this technology due to its exceptionally stringent vibration testing requirements and the need for sophisticated control systems when testing satellites. The aerospace industry imposes the most rigorous vibration testing standards globally, necessitating advanced control systems to ensure accurate reproduction of operational loads and precise boundary conditions. To address these challenges and prevent undesirable coupling between the shaker table and the Item Under Test (IUT), extensive research has been conducted on Multiple-Input and Multiple-Output (MIMO) control systems. Key contributions in this field include works by Peeters [28], De Bruyne [11], Ayres [8], Underwood [30] and Musella [26, 27]. These endeavors have paved the way for multiaxial shakers to meet the exacting demands of aerospace vibration testing, ensuring the reliability and structural integrity of critical components such as satellites.

1.3. Illustration of load severity comparison

To underscore the significance and practical utility of load severity comparison, an example from the realm of space engineering is presented. During a spacecraft's (SC) launch, it is subjected to mechanical vibrations introduced by the LV through the LV-SC IF. These vibrations emanate from various sources, including propulsion forces, aerodynamic forces, and acoustic and shock loads. These mechanical vibrations can be categorized as follows:

- Sinusoidal vibrations, ranging from 5 to 100 Hz
- Random vibrations, spanning from 20 to 2000 Hz
- Shock loads, extending from 100 to 10000 Hz

Among the myriad sources of random vibrations, acoustic loads generated within the fairing are particularly common. Their frequency range falls between 20 and 8000 Hz, with specific interest limited to the $20 - 2000$ Hz range, as frequencies beyond 2000 Hz fall within the domain of shock loads.

Figure 1.1, which focuses on a mono-axial direction, shows the measurement of the Acceleration Power Spectral Density (APSD) with a red dashed line, obtained from a unit subjected to acoustic loads during a qualification test. The latter is compared to the APSD of the unit's qualification random profile, depicted with a black dashed line. The measured APSD exhibits some peaks that exceed the unit's qualification level, but as the APSD is a density, it cannot provide insights into whether these peaks pose a problem or not. Consequently, the ERS, representing the severity of random loads, must be calculated for both the measured APSD and the random qualification level.

The figure also displays the severities of the APSD curves, which are given by the ERSs, with continuous lines in the same color as their respective APSD. The ERS is given by the acceleration which is exceeded only once over the duration of the random loading. Narrow peaks in the APSD have a minimal impact on the severity. Nevertheless, there remains a peak in the ERS of the measured data that exceeds the ERS of the qualification profile. One might consider the need for delta qualification[1] for the unit.

The figure further presents the sine qualification profile for the unit and the shock qualification profile, each with its respective severity which is given by the SRS. For each frequency f, the SRS is given by the maximum absolute acceleration calculated by applying a deterministic acceleration time history to a SDOF system with natural frequency $f_n = f$. The SRS of the sine profile is indeed is approximated by multiplying the sine's amplitude by the qualification factor Q, while the shock qualification's severity is represented by the SRS of the shock itself. Notably, the ERS of the APSD for the measured acoustic loads is enveloped by the SRS of the unit's shock qualification profile. This is encouraging in order to believe that no damage nor degradations occurred after the acoustic test.

This example vividly illustrates the value of being able to assess and compare the severity of mechanical loads of diverse natures. Additionally, the fact that the SRS of the unit's shock qualification profile partially encompasses the ERS of the measured load underscores the critical importance of accurate methodologies for evaluating severities.

[1]Delta qualification: qualification performed on an equipment which has undergone minor design modifications or has been qualified to operate in environments less severe than those specified. (Source: ECSS [3]).

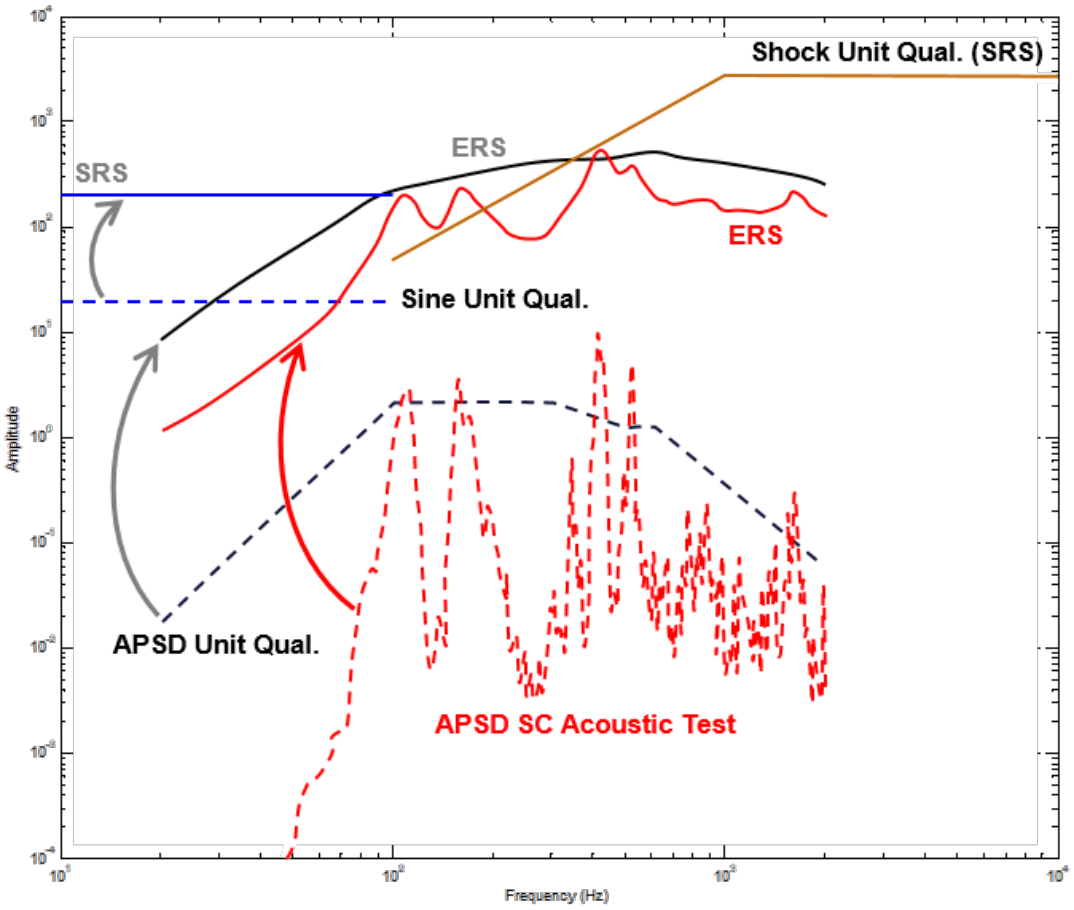

Figure 1.1: Example of mechanical load severity comparison application.

2 | Shock Response Spectrum (SRS)

2.1. Overview

This chapter begins by delving into the world of engineering shocks. It defines what shocks are and provides real-world examples to illustrate their significance across various engineering domains. This foundational understanding sets the stage for a deeper exploration of shock analysis and assessment.

The chapter introduces the SRS, a crucial tool for quantifying shock severity. This metric helps engineers gauge the impact and potential consequences of shock events, aiding informed decision-making in design and evaluation processes.

A significant portion of the chapter is dedicated to examining methodologies commonly used in the industry to evaluate the SRS. These methodologies are analyzed in-depth, highlighting their respective strengths and weaknesses. The chapter also provides a comparative assessment, addressing factors like accuracy and computational cost, empowering readers to choose the most suitable approach for their specific shock analysis needs.

Practical application comes into play within the field of space engineering, where the concept of the Equivalent Sine Input (ESI) takes center stage. A 2DOF mechanical system serves as a case study to assess whether ESI effectively represents the severity of Coupled Load Analysis (CLA). This application underscores the real-world importance of SRS analysis, particularly in assessing and ensuring the structural integrity of satellites and SC subjected to the rigors of space travel.

In summary, this chapter offers a comprehensive journey through the realm of shock analysis. It provides readers with the knowledge and tools required to assess shock severity, comprehend shock response spectra, and make informed decisions in engineering scenarios where shocks play a crucial role.

2.2. Shock

A shock is an abrupt and intense transient motion characterized by its high frequency and amplitude. In the realm of engineering, mechanical shocks can manifest in various scenarios, notably within aerospace [5] and defense [2] engineering. Although a shock may not directly inflict damage upon the primary structure of a military aircraft or a satellite, it poses a significant risk to electronic and optical components, potentially resulting in partial or complete mission failure. Throughout the lifecycle of SC, they are exposed to shocks originating from multiple sources. These include events such as the separation of LV stages, the detachment of the SC from the final stage, engine burn-ups, and the release of appendages. Furthermore, shocks can arise during transportation if the SC is transported on a truck that encounters speed bumps or traverses railroad tracks at high velocities.

2.3. Measure of a shock

To ensure the durability of designed components against mechanical shocks, it is imperative to subject them to rigorous laboratory testing. However, accurately representing shocks using a mathematical function proves exceedingly challenging. Consequently, engineers require alternative tools to comprehend the impact of shocks on SC components. In 1932, Biot [9] proposed a groundbreaking metric known as the SRS in his thesis, which originally focused on studying the effects of earthquakes on buildings. This metric serves as a means to quantify shock severity. Today, numerous shock design and test methods, such as those outlined in ECSS and MIL standards [2, 5], rely on the SRS as a guiding principle. The principle of the SRS extends beyond just measuring the severity of shock-induced mechanical loads. It is a versatile concept that can be effectively employed to assess the magnitude of transient mechanical forces, including those of middle to low frequencies, as well as deterministic vibrations.

2.4. How to compute the SRS

Biot's metric involves applying the load under consideration to a standardized mechanical system. This system comprises a support structure and N linear SDOF mass-spring-damper systems. Each system has a distinct stiffness (k_i) but shares the same damping coefficient. The next step involves evaluating the maximum absolute response quantity of each system and plotting it against the corresponding natural frequencies. A visual representation of this process can be found in Figure 2.1.

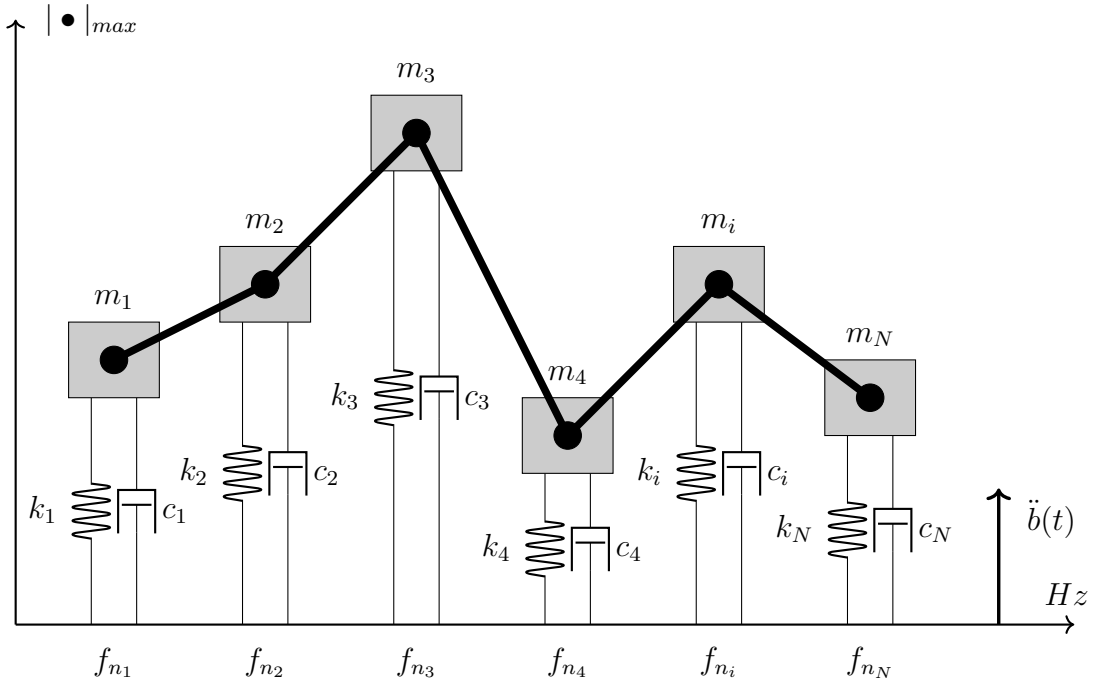

Figure 2.1: Conceptual scheme for evaluating the SRS.

To obtain a specific vector of natural frequencies, the k_i and m_i pairs are adjusted accordingly. One commonly employed scheme, as used by Irvine [18], is a proportional bandwidth such as 1/6. This means that a natural frequency is equal to the previous one multiplied by $2^{\frac{1}{6}}$. In this scheme, the output response at a given frequency corresponds to the exact value for that frequency, while the values between two consecutive frequencies are interpolated. This interpolation allows for a smooth representation of the SRS across the frequency range of interest. Additionally, the damping coefficient c_i is chosen such that the resulting quality factor $Q = 10$. This choice of Q is a convention used to enable meaningful comparisons between the severities of different loads. It is crucial to note that comparing response spectra evaluated with varying quality factors would lack significance and would not yield valuable insights or conclusions. Therefore, standardizing the quality factor at $Q = 10$ ensures a consistent basis for comparing different severities. Within the aerospace industry, the absolute acceleration serves as the predominant output parameter for evaluating shock response. It is important to note that the response can be either positive or negative, but their magnitudes should be equal. This equality of positive and negative responses ensures the accuracy and validity of the spectrum. When constructing the SRS, the maximum absolute value is selected from the positive and negative responses. This choice allows for capturing the most significant response magnitude, regardless of its polarity. By considering the maximum absolute value, the SRS effectively represents the

peak response experienced by the system, providing valuable insights into the severity of the shock.

To derive the absolute acceleration of a SDOF system, consider the generic spring-mass-damper system depicted in Figure 2.2.

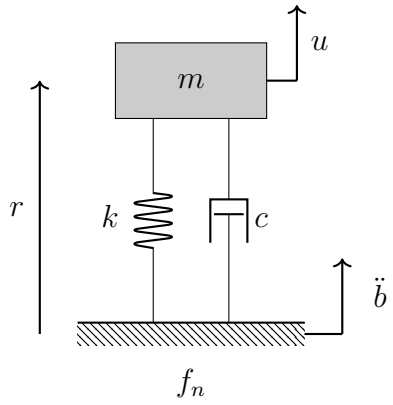

Figure 2.2: Spring-mass-damper system.

The equation of motion can be written as

$$m\ddot{u} + c(\dot{u} - \dot{b}) + k(u - b) = 0 \tag{2.1}$$

By introducing the relative displacement

$$r = u - b \tag{2.2}$$

which denotes the displacement between the mass and the base, the equation can be rearranged to express it in terms of the relative displacement

$$m\ddot{r} + c\dot{r} + kr = -\ddot{b} \tag{2.3}$$

Utilizing the definitions of the circular frequency ω_n and the dimensionless damping ratio ξ, equation 2.4 is obtained through rearrangement.

$$\ddot{r} + 2\xi\omega_n\dot{r} + \omega_n^2 x = -\ddot{b} \tag{2.4}$$

2.4.1. Matlab integration

An effective and direct method to solve Equation 2.4 is to utilize a MATLAB built-in function such as *lsim*. In this context, the solution - the relative displacement x -

is the exact outcome. Upon multiplying the relative displacement by w_n^2, the relative acceleration or static acceleration $\ddot{x}$ can be obtained. By utilizing the relationship in Equation 2.2, the absolute acceleration $\ddot{u}$ can then be derived.

2.4.2. Craig's recurrence formulas

An alternative technique involves utilizing the recurrence formulas outlined in Craig [10]. This approach relies on a piecewise-linear interpolation of both the forcing acceleration and the exact solution. The recurrence formulas for the underdamped SDOF system are expressed as follows:

$$u_{i+1} = Ap_i + Bp_{i+1} + Cu_i + D\dot{u}_i \tag{2.5}$$

$$\dot{u}_{i+1} = A'p_i + B'p_{i+1} + C'u_i + D'\dot{u}_i \tag{2.6}$$

where $p = -\ddot{b}$ and the coefficients can be found in Appendix A.1.

2.4.3. Smallwood's recursive formula

The Smallwood's recursive formula for simulating the SDOF system is based on a digital recursive filter. The output of the filter represents the response of the SDOF system. Smallwood's technique is an improvement over the Kelly-Richman method and incorporates a ramp invariant technique. The recursive formula can be expressed as follows:

$$\ddot{u}_i = b_0\ddot{p}_i + b_1\ddot{p}_{i-1} + b_2\ddot{p}_{i-2} - a_1\ddot{u}_{i-1} - a_2\ddot{u}_{i-2} \tag{2.7}$$

where $p = -\ddot{b}$ and the coefficients can be found in Appendix A.2.

This technique provides a computationally efficient way to simulate the response of the SDOF system.

2.5. Comparing methodologies for SRS analysis

In this section, we present a comprehensive comparison of three distinct methodologies employed for SRS analysis. The objective is to elucidate the differences and nuances among these methods. For the comparison, a set of SDOF systems was subjected to a unitary step function, assuming an infinite quality factor (Q) corresponding to $\xi = 0$. This choice is motivated by the well-known fact that the maximum absolute response of

an undamped SDOF system to a unitary step function is 2. A total time span of 0.7 seconds was considered for the unitary step.

The SRS assessment was performed by selecting natural frequencies for the array of SDOF systems, starting from 1 Hz and progressively increasing with a proportional bandwidth of $1/96$, culminating at a final frequency of $\frac{1}{dt\,8}$, which is the sampling frequency divided by 8. Two separate analyses were carried out: one utilizing a time step of $10^{-4}s$ and another employing a finer time step of $10^{-5}s$ to discern the impact of time step choice on the computational cost across methodologies.

The comparison's graphical representation for the $10^{-4}s$ time step can be observed in Figure 2.3. Analysis reveals that both the lsim integration and the Craig recurrence formulas yield exact solutions. Conversely, Smallwood's recursive formula approach exhibits deviation from the exact solution as natural frequencies increase. This discrepancy arises from Smallwood's algorithm assuming zero initial conditions, effectively treating the first input value of the unitary step as 0.

The relative error between the three algorithms and the analytical solution, which is 2, is shown in Figure 2.4. Notably, at 1250 Hz, the relative error stands at around 1.3%, a significant deviation for comparison purposes. A potential solution to mitigate this issue involves reducing the time step to $10^{-5}s$, thereby allowing a maximum SDOF array frequency of 12500 Hz. This refinement is evident in Figures 2.5 and 2.6, effectively reducing the error. However, this refinement comes at the expense of increased computational demands when evaluating the SRS.

Furthermore, a detailed examination of the computational costs associated with each methodology is provided in Tables 2.1, 2.2. These costs are normalized with respect to lsim integration. Smallwood's recursive formula stands out as the most computationally efficient option. Additionally, it's important to highlight the influence of time step on the relative computational costs of the Craig and Smallwood methods. As the time step is reduced, the ratio between the computational cost of the Craig method compared to the Smallwood method experiences a noticeable increase. This dynamic sheds light on the intricate relationship between time discretization and the computational efficiency trade-offs inherent in these methodologies.

Table 2.1: Computational cost of the different methods, normalized with respect to the lsim integration. Time step = $10^{-4}s$.

Method	Computational Cost
lsim	1
Craig	0.070
Smallwood	0.026

Table 2.2: Computational cost of the different methods, normalized with respect to the lsim integration. Time step = $10^{-5}s$.

Method	Computational Cost
lsim	1
Craig	0.118
Smallwood	0.041

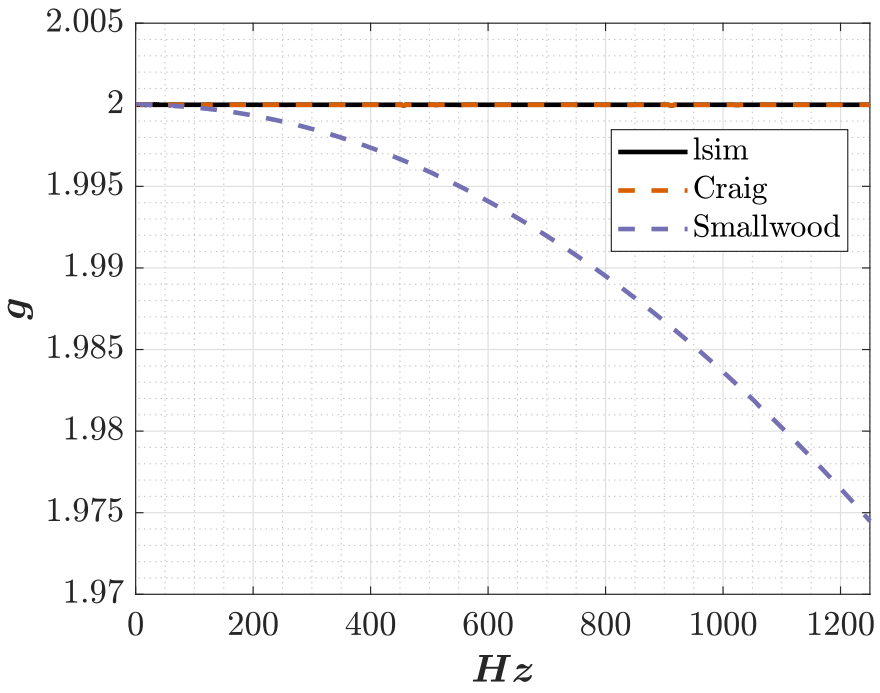

Figure 2.3: Comparison of methodologies for SRS analysis. Time step = $10^{-4}s$.

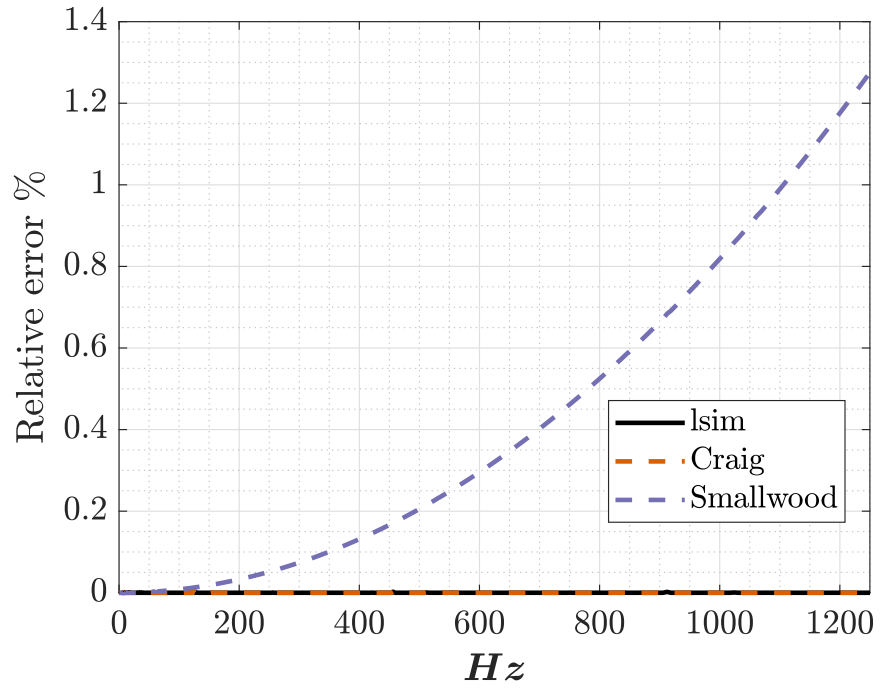

Figure 2.4: Relative error compared to the analytical solution. Time step = $10^{-4}s$.

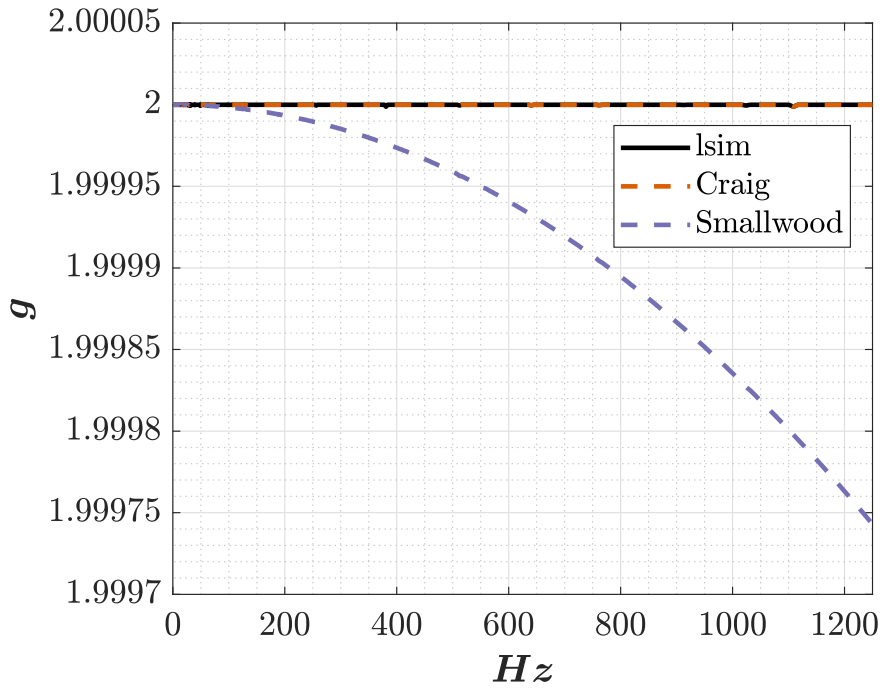

Figure 2.5: Comparison of methodologies for SRS analysis. Time step = $10^{-5}s$.

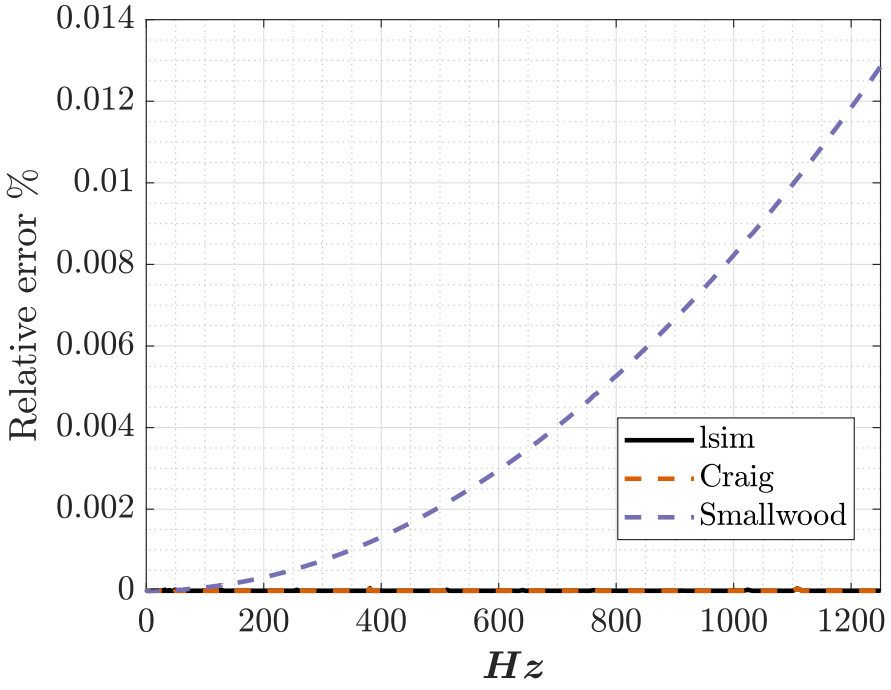

Figure 2.6: Relative error compared to the analytical solution. Time step = $10^{-5}s$.

2.6. SRS applications in space engineering

Satellite structures undergo rigorous testing to ensure their robustness in the face of challenging mission conditions. These evaluations often involve subjecting the satellites to qualification tests, which simulate the mechanical stresses experienced during a mission. These tests are pivotal in verifying whether a satellite can withstand the demands of its operational environment.

One of the primary tools used for such testing is the shaker. Shakers are designed to replicate real-world conditions by applying controlled vibrations and forces to the satellite structures. Within the context of the space industry, electrodynamic and hydraulic shakers are commonly utilized for these tests. It's crucial to highlight that current shaker systems still face limitations in effectively replicating a 6DOF transient load. Therefore, to comprehensively replicate the complex load conditions encountered in space missions, multiple mono-axial excitation runs are often performed.

These excitation runs employ a sinusoidal sweep technique, where the frequency of excitation increases gradually over time. This sweep function is defined by the equation:

$$a_{sw}(t) = \sin\left(2\pi \frac{60 f_0}{K_e ln(2)} \left(2^{(K_e/60)t} - 1\right)\right) \tag{2.8}$$

Here, K_e represents the sine sweep rate, typically set at 2 octaves per minute for qualification tests and 4 octaves per minute for acceptance tests.

Notably, sine vibration tests performed during shaker tests represent a critical phase in a satellite's development life cycle. The qualification levels for these excitations are outlined in Launch Vehicle User's Manuals (LVUMs), which serve as guiding documents for conducting these tests. An example of such qualification levels is presented in Table 2.3.

Table 2.3: Vega-C Sinusoidal vibration test levels for single launch configuration [6].

Sine	Frequency Range [Hz]	Qualification Levels (0-peak)
Longitudinal	1-5	10 mm
	5-35	1.00 g
	35-110	1.25 g
Lateral	1-5	10 mm
	5-30	1.00 g
	30-110	0.625 g

During the course of these sweep tests, the frequencies encountered inevitably coincide with the resonant frequencies of the satellite structure. However, these resonances are not representative of mission conditions due to their transient nature. To address this, a process known as notching is employed to ensure that the input test levels align with actual mission conditions.

Primary notching involves adjusting the input levels within frequency ranges where the force or moment at the LV-SC IF might exceed mission-experienced levels. This information is derived from Quasi-Static Loads (QSLs) as specified in LVUMs. However, in cases where payload or instrument accelerations during testing surpass their qualified limits, a secondary notching process is implemented. Care must be taken to ensure that secondary notching does not interfere with the primary notching, as it could potentially lead to an underestimation of the satellite's ability to withstand mission conditions.

A key parameter in this process is the ESI, as defined by ECSS [4].

"Let us consider a SDOF system having a natural frequency f_k and being excited at the base with a transient acceleration $\ddot{u}(t)$. The equivalent sine input $ESI(f^*)$ at a generic frequency f^*, $\ddot{u}(t)$, can be defined as the amplitude of the sinusoidal acceleration at the base, with an excitation frequency equal to f^*, which makes the SDOF system with natural frequency $f_k = f^*$ reach, at steady-state condition, the acceleration amplitude $SRS(f^*)$ which is the SRS of $\ddot{u}(t)$ at the frequency f^*."

In this context, the transient load $\ddot{u}(t)$ (in this thesis $\ddot{b}(t)$) is derived from the LV-SC CLA, a dynamic analysis meticulously executed by the launch authority. The primary objective of this analysis is to simulate the entirety of the flight events, comprehensively evaluating whether the SC aligns with the stringent requirements outlined in the LVUMs.

The ESI, acting as a representative indicator of the severity encapsulated within the CLA, assumes a pivotal role in guiding the secondary notching process. This critical parameter establishes a lower threshold that guarantees the satellite's instruments and equipment experience accelerations that are, at the very least, on par with those projected during the actual mission.

The steps to retrieve the ESI are:

1. Perform a transient analysis for each frequency in the range $f \in [1 - 110]\ Hz$ for the SDOF system.
2. Calculate the SRS curve by determining the maximum absolute response (acceleration $\ddot{u}$) for each frequency:

$$SRS(f) = \max_t \|\ddot{u}(t, f)\| \tag{2.9}$$

3. Compute the ESI curve by dividing SRS by $\sqrt{Q^2 + 1}$, where $Q = \dfrac{1}{2\xi}$ represents the quality factor indicating the system's amplification when subjected to unit base motion, and ξ is the modal damping ratio. For this context, Q is set at $Q = 25$, corresponding to a damping ratio $\xi = 2\%$. For high Q values, $\sqrt{Q^2 + 1} \approx Q$.

$$ESI = \frac{SRS}{\sqrt{Q^2 + 1}} \tag{2.10}$$

A simulated axial-symmetric satellite model was constructed using FEMAP. Subsequently, predictions for sine tests and critical load analyses (CLA) were conducted utilizing MSC Nastran. Figure 2.7 provides insight into the prediction results of the sine test, illustrating the input profile, SC IF lateral moment (M_Y), and payload acceleration. As depicted in Figure 2.7b, the input level from LVUM results in an SC IF lateral moment exceeding the value derived from QSLs. Consequently, the input level is notched (red curve). Even after primary notching, as seen in Figure 2.7c, payload acceleration remains higher than its qualification level, necessitating secondary notching (yellow curve). The ESI (gray curve) in Figure 2.7a functions as a lower bound for secondary notching. Should the notch for secondary notching fall below the ESI curve, payload acceleration during testing would be lower than that during the CLA.

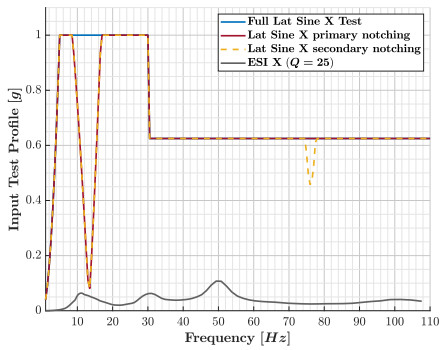

(a) Sine X: Input profile.

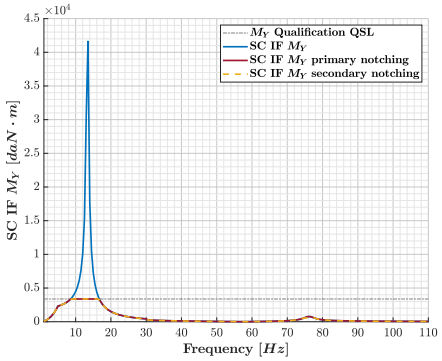

(b) Sine X: SC IF lateral moment M_Y.

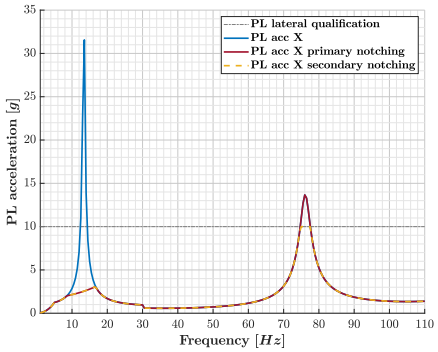

(c) Sine X: PL acceleration.

Figure 2.7: Sine X test prediction results.

2.7. ESI for a 2DOF system

To assess the applicability and accuracy of the ESI concept, a MATLAB-based 2DOF system was meticulously developed. This analysis serves as an essential validation step, aiming to ascertain whether the ESI effectively captures the true severity of the CLA. The study encompasses both a modal analysis and a transient analysis. To extend the study's relevance, a parametric analysis was conducted, systematically varying system parameters to examine their influence on the obtained outcomes.

Consider the 2DOF system depicted in Figure 2.8, which offers insight into the dynamic interaction between various components:

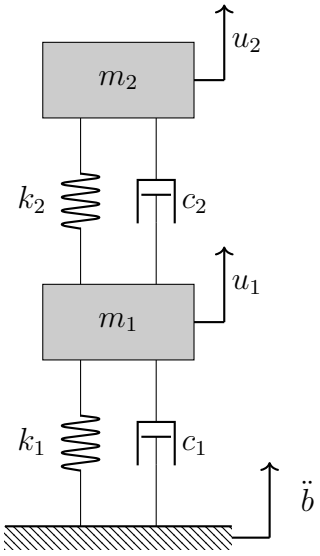

Figure 2.8: 2DOF Spring-mass-damper system.

Notably, while the current analysis focuses on longitudinal displacements, the principles outlined remain applicable when dealing with lateral displacements as well. The subscripts 1 and 2 represent a SC and a telescope (TS), respectively.

It's important to highlight that the base of the system corresponds to the connection point between the LV and the SC, commonly referred to as the LV-SC IF. This IF plays a pivotal role in transmitting dynamic loads from the LV to the SC structure.

The system's stiffness and damping coefficients (k_i and c_i) are computed based on the respective masses and natural frequencies of SC and TS:

$$k_i = m_i(2\pi f_i)^2 \tag{2.11}$$

$$c_i = \xi \cdot 2\sqrt{k_i m_i} \tag{2.12}$$

where $\xi = \frac{1}{2Q}$, and the quality factor (Q) is set to 25.

The dynamic behavior of the 2DOF system can be represented by a set of equations of motion, conveniently organized in matrix form as presented in Equation 2.15:

$$\begin{bmatrix} m_2 & 0 & 0 \\ 0 & m_1 & 0 \\ 0 & 0 & 0 \end{bmatrix} \begin{Bmatrix} \ddot{u}_2 \\ \ddot{u}_1 \\ \ddot{b} \end{Bmatrix} + \begin{bmatrix} c_2 & -c_2 & 0 \\ -c_2 & c_1 + c_2 & -c_1 \\ 0 & -c_1 & c_1 \end{bmatrix} \begin{Bmatrix} \dot{u}_2 \\ \dot{u}_1 \\ \dot{b} \end{Bmatrix} + \begin{bmatrix} k_2 & -k_2 & 0 \\ k_2 & k_1 + k_2 & -k_1 \\ 0 & -k_1 & k_1 \end{bmatrix} \begin{Bmatrix} u_2 \\ u_1 \\ b \end{Bmatrix} = \begin{Bmatrix} 0 \\ 0 \\ F_B \end{Bmatrix} \tag{2.13}$$

This equation encapsulates the dynamic interactions between the masses, springs, and dampers within the system. Here, m_1 and m_2 denote the masses, k_1 and k_2 are the spring constants, and c_1 and c_2 represent the damping coefficients. The acceleration $\ddot{b}$ is the base excitation applied to the system.

Moreover, the equation can be reformulated in a block matrix format, highlighting the internal DOFs (denoted by I) and the boundary DOF (denoted by B):

$$\begin{bmatrix} \underline{\underline{M}}_{II} & \underline{M}_{IB} \\ \underline{M}_{IB}^T & M_{BB} \end{bmatrix} \begin{Bmatrix} \underline{\ddot{u}}_I \\ \ddot{u}_B \end{Bmatrix} + \begin{bmatrix} \underline{\underline{C}}_{II} & \underline{C}_{IB} \\ \underline{C}_{IB}^T & C_{BB} \end{bmatrix} \begin{Bmatrix} \underline{\dot{u}}_I \\ \dot{u}_B \end{Bmatrix} + \begin{bmatrix} \underline{\underline{K}}_{II} & \underline{K}_{IB} \\ \underline{K}_{IB}^T & K_{BB} \end{bmatrix} \begin{Bmatrix} \underline{u}_I \\ u_B \end{Bmatrix} = \begin{Bmatrix} \underline{0} \\ F_B \end{Bmatrix} \tag{2.14}$$

Where $\ddot{u}_B = \ddot{b}$. Reordering the terms the first equation yields:

$$\underline{\underline{M}}_{II}\underline{\ddot{u}}_I + \underline{\underline{C}}_{II}\underline{\dot{u}}_I + \underline{\underline{K}}_{II}\underline{\dot{u}}_I = -\underline{M}_{IB}\ddot{u}_B - \underline{C}_{IB}\dot{u}_B - \underline{K}_{IB}u_B \tag{2.15}$$

This rearrangement isolates the contributions of internal DOFs ($\underline{\ddot{u}}_I$ and $\underline{\dot{u}}_I$) and boundary DOFs ($\ddot{u}_B$, $\dot{u}_B$, and u_B), providing a clearer insight into the system's dynamic interactions.

The study of the 2DOF system involves a comprehensive investigation through two distinct yet interrelated analyses: a modal analysis and a transient analysis. These analyses provide valuable insights into the system's behavior under varying conditions. The analytical process is succinctly depicted in Figure 2.9, showcasing the sequence of steps involved in both analyses.

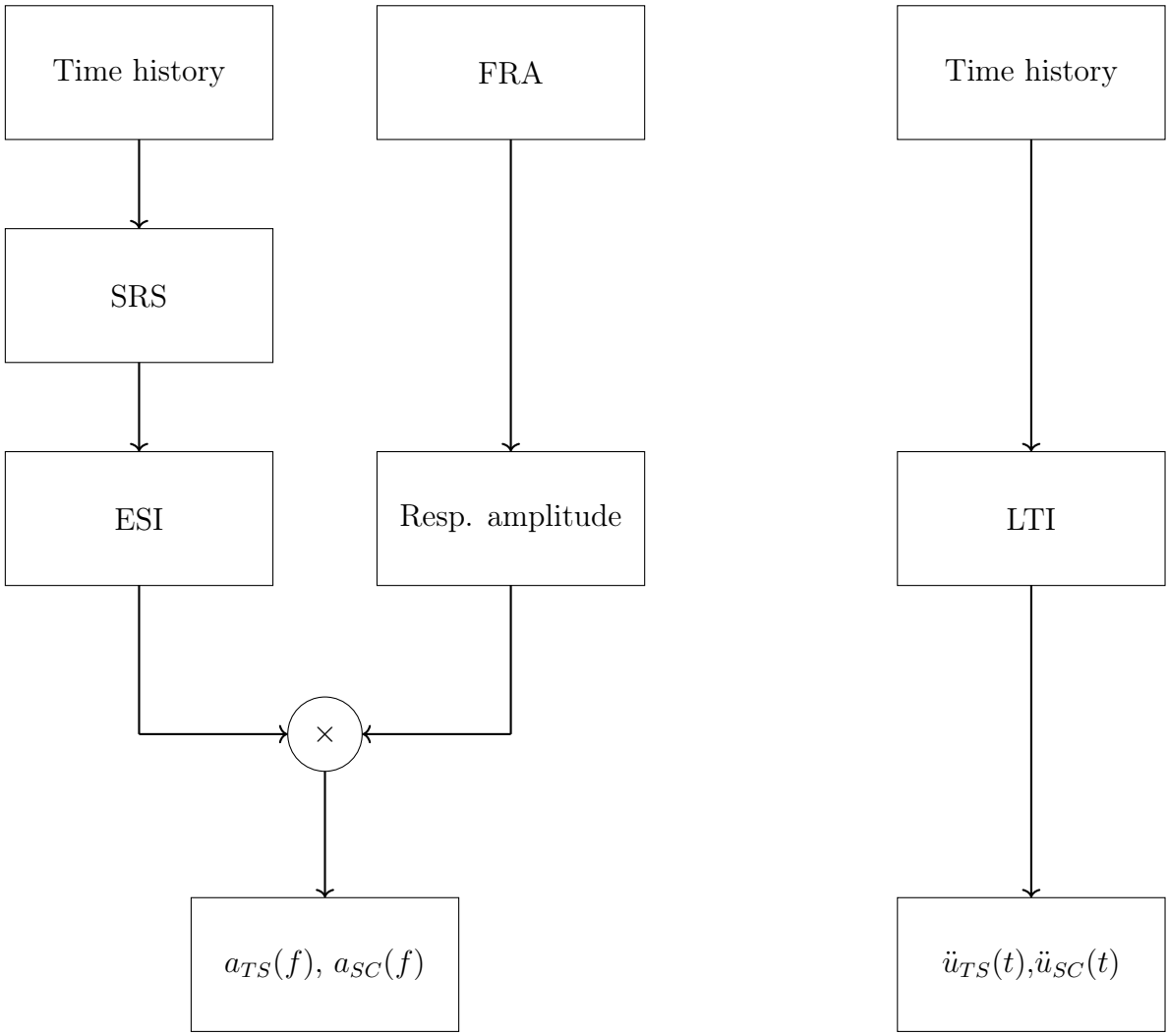

Figure 2.9: Analyses workflow: modal analysis (left) and transient analysis (right).

2.7.1. Transient analysis

The transient analysis of the 2DOF system offers a comprehensive insight into its behavior when subjected to real-world transient events. In this analysis, the system's base is subjected to the acceleration time history retrieved from the CLA, reflecting actual dynamic conditions. The primary objectives of this analysis are to calculate the acceleration time histories of both the SC and the TS masses, determine their maximum values, and subsequently compare these results with those obtained from the modal analysis. This comparison serves as a critical assessment of the system's transient response and natural behavior.

The governing Equation 2.15 is conveniently transformed into state-space form to facilitate the analysis:

$$\dot{\underline{\bar{x}}} = \begin{bmatrix} \underline{\underline{0}} & \underline{\underline{I}} \\ -\underline{\underline{M}}_{II}^{-1}\underline{\underline{K}}_{II} & -\underline{\underline{M}}_{II}^{-1}\underline{\underline{C}}_{II} \end{bmatrix} \underline{\bar{x}} + \begin{bmatrix} \underline{\underline{I}} & \underline{\underline{0}} \\ \underline{\underline{0}} & -\underline{\underline{M}}_{II}^{-1} \end{bmatrix} \begin{Bmatrix} \underline{0} \\ \underline{F} \end{Bmatrix} \tag{2.16}$$

$$\underline{\bar{y}} = \begin{bmatrix} \underline{\underline{0}} & \underline{\underline{I}} \\ -\underline{\underline{M}}_{II}^{-1}\underline{\underline{K}}_{II} & -\underline{\underline{M}}_{II}^{-1}\underline{\underline{C}}_{II} \\ \underline{\underline{I}} & \underline{\underline{0}} \end{bmatrix} \underline{x} + \begin{bmatrix} \underline{\underline{I}} & \underline{\underline{0}} \\ \underline{\underline{0}} & -\underline{\underline{M}}_{II}^{-1} \\ \underline{\underline{0}} & \underline{\underline{0}} \end{bmatrix} \begin{Bmatrix} \underline{0} \\ \underline{F} \end{Bmatrix} \tag{2.17}$$

In these equations, $\underline{F} = -\underline{M}_{IB}\ddot{u}_B - \underline{C}_{IB}\dot{u}_B - \underline{K}_{IB}u_B$, where $\ddot{u}_B$ represents the known acceleration time history from the CLA. By integrating this time history using the MATLAB function *cumtrapz*, the values of $\dot{u}_B$ and u_B can be obtained. The system's response is then determined using the MATLAB function *lsim*.

2.7.2. Modal analysis

The modal analysis serves as a representative simulation of satellite tests conducted on a shaker, which are crucial to understanding the system's response to various vibrational loads. This analysis involves a Frequency Response Analysis, where the frequency range of $5 - 110, \mathrm{Hz}$ is meticulously chosen. The base of the 2DOF system is subjected to a unitary acceleration excitation, enabling an exploration of the system's behavior across the chosen frequency spectrum.

The governing Equation 2.15 can be transformed into the frequency domain to facilitate the modal analysis:

$$-\underline{\underline{M}}_{II}\omega^2\underline{u}_I + \underline{\underline{C}}_{II}j\omega\underline{u}_I + \underline{\underline{K}}_{II}\underline{u}I = +\underline{M}_{IB}\omega^2 u_B - \underline{C}_{IB}j\omega u_B - \underline{K}_{IB}u_B \tag{2.18}$$

By setting $-\omega^2 u_B = 1$, the 2DOF system is subjected to a unitary acceleration in the frequency domain. This procedure allows the acceleration of the two masses to manifest as the transmissibility, offering insight into how each mass responds at different frequencies.

For each mass, the magnitude of the response acceleration is plotted against its corresponding frequency within the chosen frequency range. This representation provides a comprehensive understanding of the system's frequency-dependent behavior.

In continuation, the Structural Response Spectrum (SRS) of the acceleration time history utilized to drive the base of the 2DOF system in the transient analysis is computed. Furthermore, the ESI is evaluated through Equation 2.10. The ESI serves as a crucial metric that quantifies the severity of the CLA.

Then, the SRS of acceleration time history used to enforce the base of the 2DOF system in the transient analysis is computed, the ESI is evaluated through Equation 2.10.

Finally, the plot derived from the Frequency Response Analysis (FRA) is scaled by the ESI.

2.8. Results

The masses and the first longitudinal frequencies of the 2DOF system were deliberately selected to match those of the SC and the TS modeled in FEMAP. Figure 2.10 visually presents the outcome of the transient analysis, offering an insight into how the system amplifies the base acceleration. This amplification translates to a higher acceleration experienced by both the SC and the TS masses. Notably, this analysis was verified by imposing a unitary step function on the 2DOF system, with the damping ratio (ξ) set to 0. The validation process confirmed that the maximum absolute acceleration of the TS was indeed 2.

The modal analysis, depicted in Figure 2.11, provides further valuable insights. The frequencies of the observed peaks, specifically $55.60, \mathrm{Hz}$ and $93.23, \mathrm{Hz}$, correspond harmoniously to the first longitudinal natural frequencies of the SC and the TS respectively. This harmonization signifies the accuracy and relevance of the modal analysis in capturing the dynamic behavior of the system.

A tabulated summary of the maximum absolute accelerations attained from both analyses is presented in Table 2.4. This table serves as a valuable comparison, highlighting the differences in acceleration between the transient and modal analyses.

Table 2.4: Maximum absolute acceleration in g of the 2DOF system.

	Transient	**Modal**
SC	11.12	11.85
TS	16.55	17.84

The results underscore the nuanced variations between the modal and transient approaches. The modal analysis, which leverages the ESI, yields slightly higher acceleration values for both the SC and TS masses. Specifically, the acceleration of the SC is elevated by approximately 6.56%, while the acceleration of the TS is augmented by approximately 7.79%.

In order to gain a deeper understanding of the system's behavior and its sensitivity to various parameters, a parametric analysis was conducted. This analysis involved systematically varying the masses and frequency values of the 2DOF system to assess how the results might change and how these changes are influenced by the system's parameters. The aim was to explore the impact of parameter variations on the differences between the modal and transient analysis results.

To facilitate this analysis, the parameters of the system were chosen to be as generalized and realistic as possible. While values for m_1, f_1, and Q were kept constant, m_2 and f_2 were allowed to vary. The collected data is summarized in Table 2.5.

Table 2.5: Data for the parametric analysis.

Element	Value
m_1	$1000\,kg$
f_1	$20\,Hz$
Q	25
m_2	$1 - 1000\,kg$
f_2	$1 - 100\,Hz$

To ensure the independence of results from the specific acceleration time history used, a deliberate choice was made to employ a unitary step function. This strategic decision was grounded in the realization that the enforcing acceleration used in the previous analysis was accurately acquired through MSC Nastran. Notably, this Nastran simulation featured a satellite embodying the exact parameters of the 2DOF system in the previous investigation.

The results of the parametric analysis were visualized through both 3D and 2D plots. Figures 2.12 and 2.14 provide contour plots illustrating the maximum absolute response difference between the modal analysis (governed by the ESI) and the transient analysis (representative of the CLA) for the TS and SC respectively. These contours vary as functions of the ratios $\frac{f_2}{f_1}$ and $\frac{m_2}{m_1}$. Evidently, there exist distinct regions where the differences are notably high.

To offer a more focused perspective, 2D plots extracted from the contours were generated. Figures 2.13 and 2.15 elucidate that as the mass ratio $\frac{m_2}{m_1}$ increases – indicating a situation where the TS mass is substantial and non-negligible – and as the frequency ratio $\frac{f_2}{f_1}$ decreases – signifying proximity of the first longitudinal natural frequencies of the TS and SC – the maximum acceleration values differ significantly between the modal and transient

analyses. This divergence highlights that the ESI doesn't precisely capture the severity of the CLA, resulting in a more conservative secondary notching effect. Consequently, this conservative approach can lead to an increase in satellite weight and subsequently its cost.

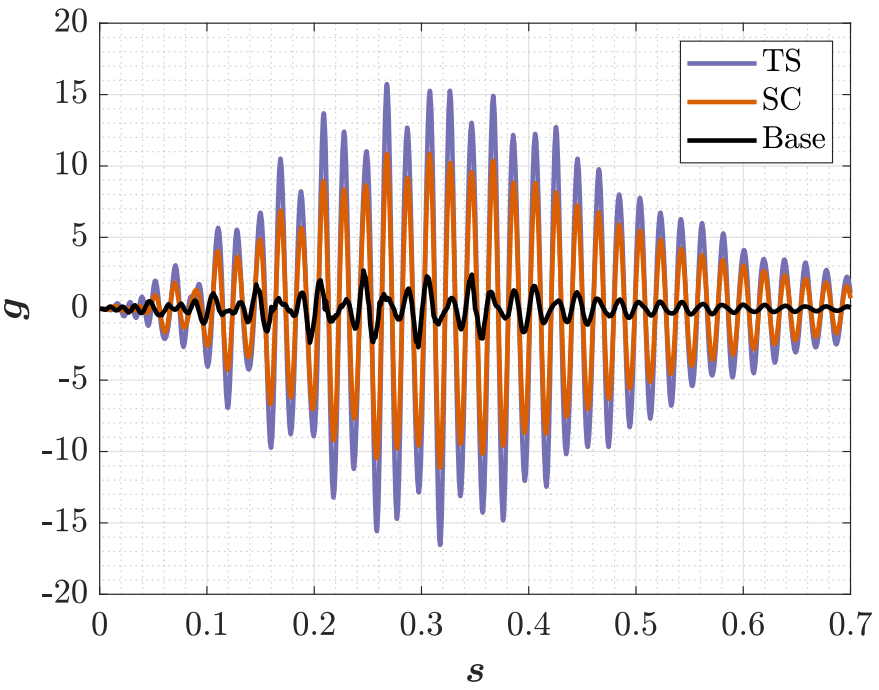

Figure 2.10: Transient analysis of the 2DOF system.

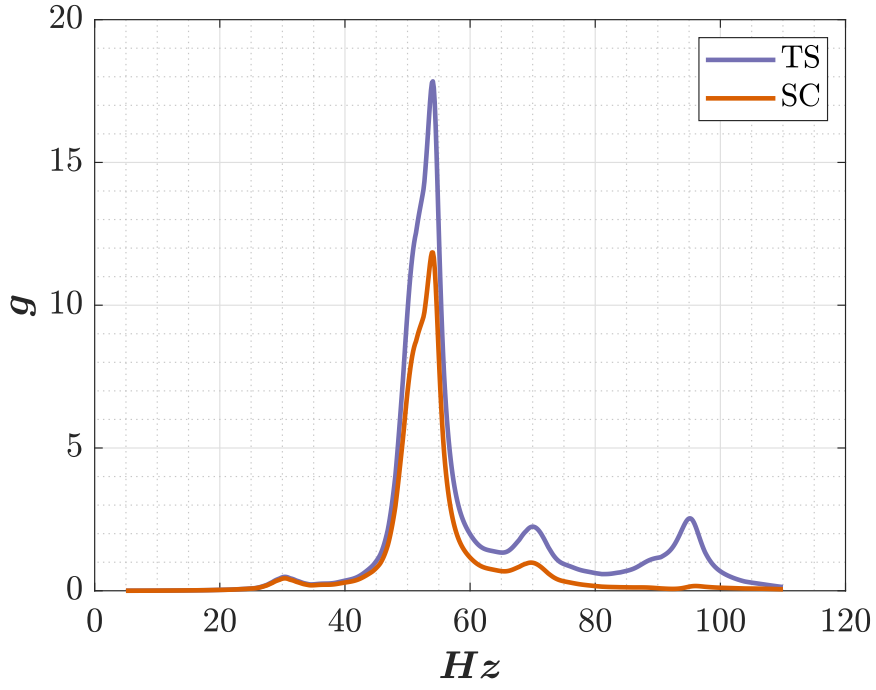

Figure 2.11: Frequency Response Analysis of the 2DOF system, scaled with ESI.

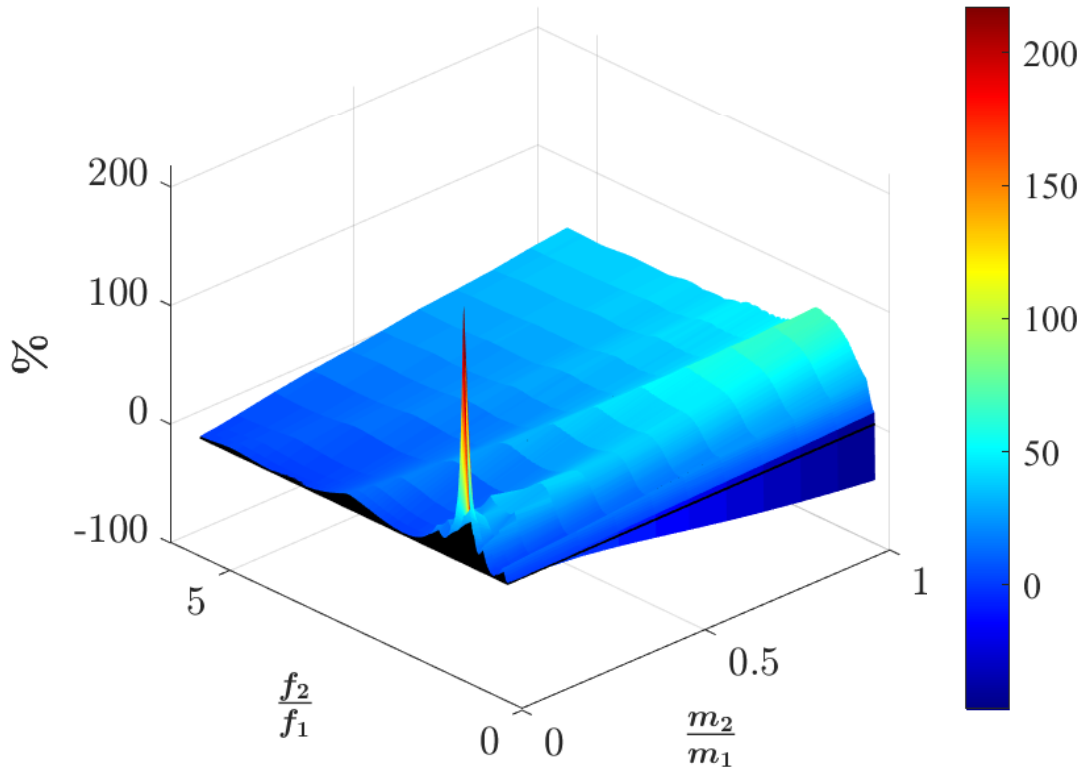

Figure 2.12: Maximal m_2 absolute response difference between ESI and CLA inputs, 3D.

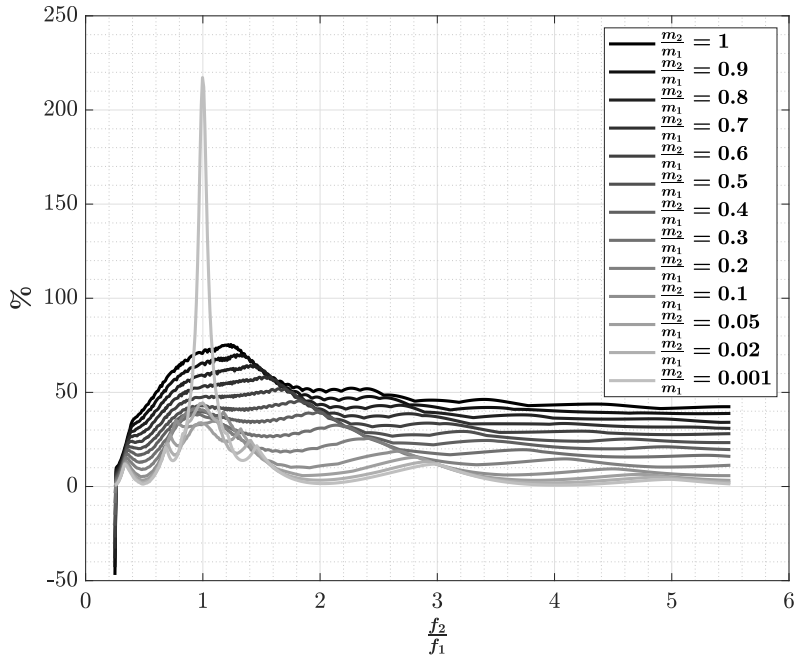

Figure 2.13: Maximal m_2 absolute response difference between ESI and CLA inputs, 2D.

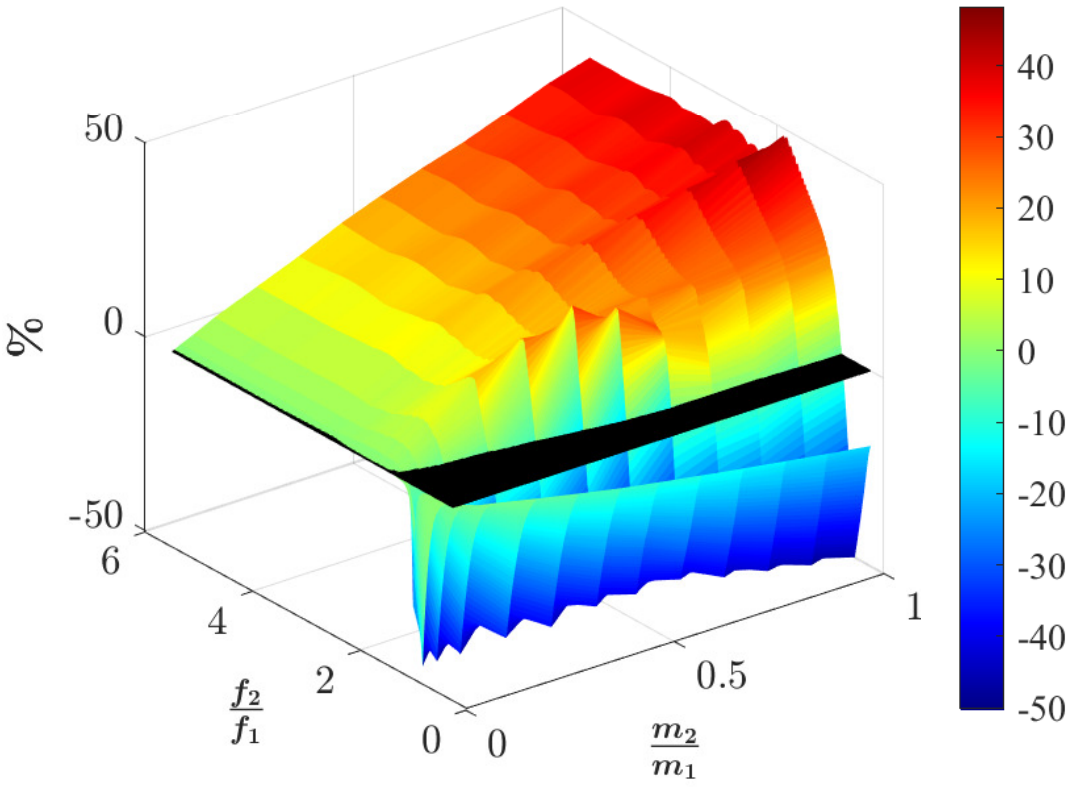

Figure 2.14: Maximal m_1 absolute response difference between ESI and CLA inputs, 3D.

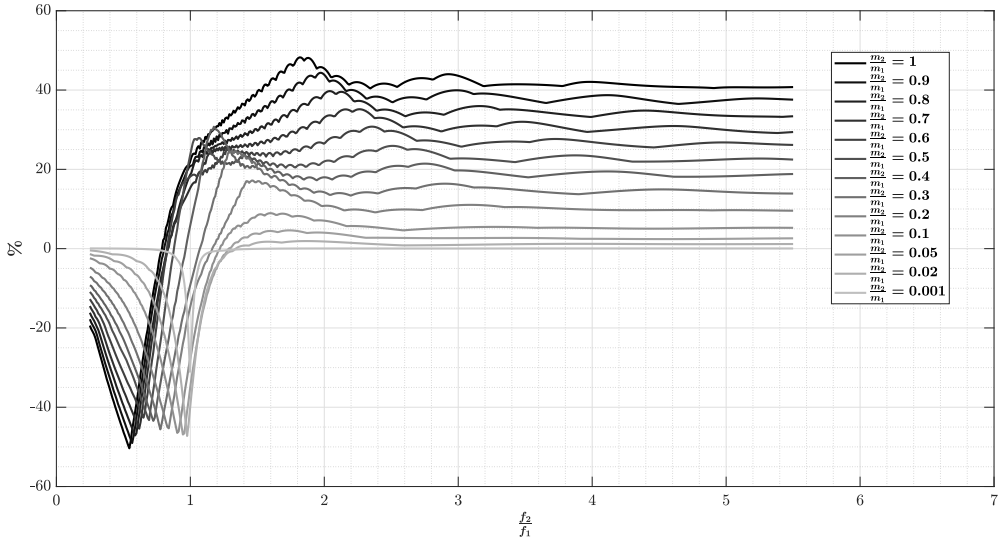

Figure 2.15: Maximal m_1 absolute response difference between ESI and CLA inputs, 2D.

3 | Extreme Response Spectrum (ERS)

3.1. Overview

This chapter commences with an introduction to random vibrations and their practical relevance in engineering. Real-world examples are provided to illustrate the impact of random vibrations on engineering systems.

Following this introduction, a fundamental metric used to quantify the severity of random vibrations is discussed, offering a basis for understanding their effects on structures and systems.

The process of obtaining the ERS, a critical tool for assessing the extreme responses of systems subjected to random vibrations, is then explained in detail.

The conventional industry methodology for ERS evaluation is explored, outlining its key aspects and limitations.

An alternative approach to ERS evaluation is subsequently introduced, with a focus on highlighting its potential advantages and applications.

To conclude the chapter, a comparison of the accuracy and computational costs of the two methodologies is presented, providing readers with practical insights for selecting the most suitable approach in the context of random vibrations and ERS evaluation.

3.2. Random vibration

Random vibration is characterized by its non-deterministic nature, meaning that its future behavior cannot be precisely predicted. As a result, quantifying and understanding random vibrations necessitates a statistical approach since it would require an infinite number of measurements to fully capture its characteristics. Within the context of SC, random loads can arise from both mechanical and acoustic sources. Mechanical random

loads manifest as vibrations transmitted from the LV to the SC through the adapter. These vibrations can be generated by combustion processes or turbulent boundary layers. While they may not pose critical design conditions for the primary structure of the SC, they significantly impact the instruments and electronic components. Acoustic loads, on the other hand, arise as pressure fluctuations with a random nature. These loads originate from sound pressure within the fairing. Acoustic loads primarily affect lightweight components with larger surface areas, such as external panels, antenna reflectors, and solar panels of the SC. In both cases, the random nature of these vibrations and acoustic loads underscores the need for a statistical approach to their characterization and analysis in the design and evaluation of SC systems.

3.3. Measure of random vibration

To conduct random testing, it is necessary to define a random test spectrum. Random vibrations are characterized by their PSD, which represents the distribution of power across different frequencies. In analogy with the SRS, the severity of the input PSD can be visualized using a curve. This curve, known as the ERS, illustrates the magnitude of the response for different frequencies. The ERS allows for a comparative analysis of the severity of random vibrations in relation to other loads, such as shocks. By plotting the ERS, engineers can gain insights into the potential maximum responses expected under random vibration conditions. This aids in the evaluation, design, and validation of systems subjected to random vibrations, enabling engineers to assess the structural integrity and performance of components and ensure they can withstand the expected dynamic loads.

3.4. How to compute the ERS

In analogy with the SRS, the computation of the ERS involves applying the PSD under consideration to a standardized mechanical system. This system consists in a support structure and in an array of N linear SDOF mass-spring-damper systems. Each system has a distinct stiffness k_i but shares the same damping coefficient. The next step involves evaluating the Root Mean Square (RMS) of the output of each system and plotting it against the corresponding natural frequencies. A visual representation of this process can be found in Figure 3.1.

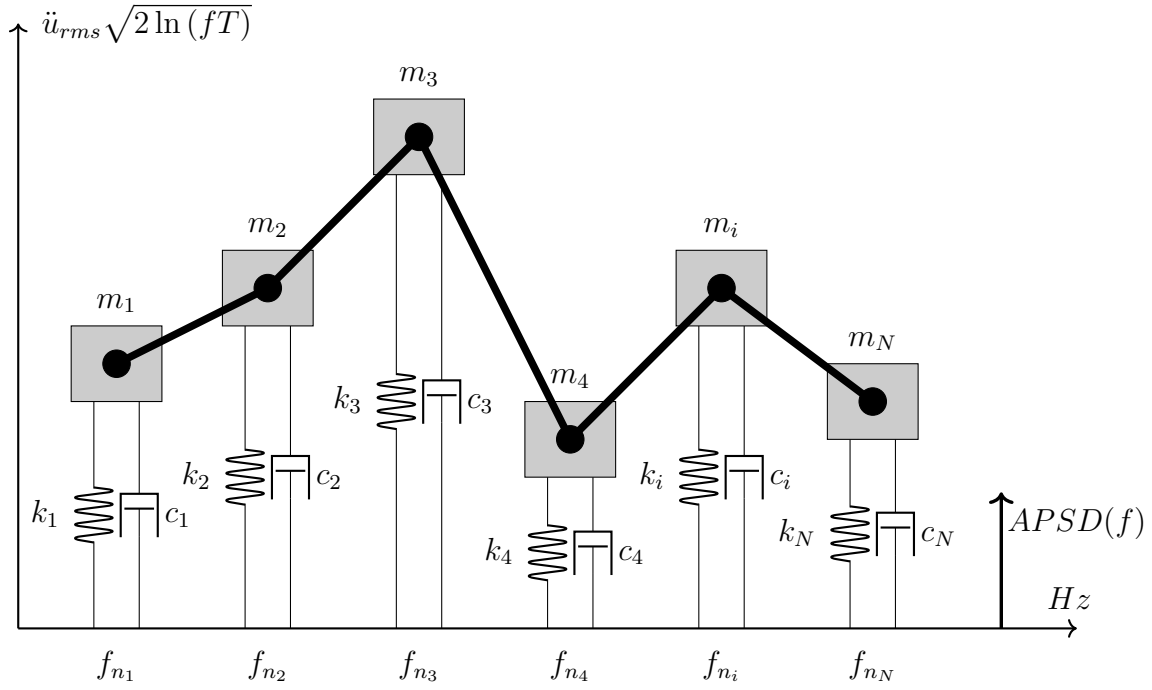

Figure 3.1: Conceptual scheme for evaluating the ERS.

As previously mentioned, the input to the mechanical system is a random vibration expressed through its PSD. This PSD can originate from real-world environmental conditions or be synthesized based on specified requirements. Evaluating the PSD from a time domain signal is beyond the scope of this thesis, but relevant techniques can be found in references [22, 31]. To characterize the output of the mechanical system, the acceleration RMS is commonly used, however it represents a mean value and not the largest peak. To further characterize the output, the acceleration RMS needs to be multiplied by the factor $\sqrt{2\ln(fT)}$ (sourced from Lalanne [23]), where T represents the duration of the random excitation. This way, the ERS is the acceleration which is only exceeded once over the duration of the random loading. The complete expression for the ERS can be found in equation 3.1.

$$ERS(f) = \ddot{u}_{rms}\sqrt{2\ln(fT)} \tag{3.1}$$

To derive the acceleration RMS of a SDOF system, consider the generic spring-mass-damper system depicted in Figure 3.2.

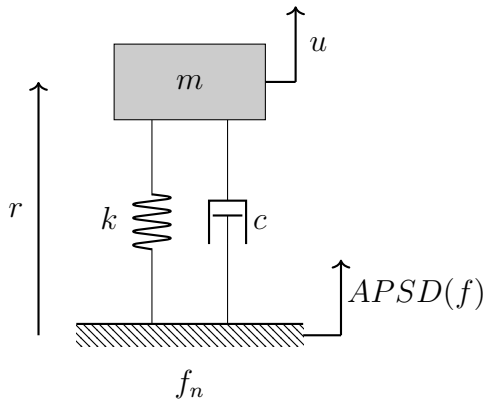

Figure 3.2: Spring-mass-damper system.

3.4.1. Integral of the transmissibility approach

The output acceleration RMS can be evaluated using the following formula:

$$\ddot{u}_{rms} = \sqrt{\int_{f\_range} |SDOF\_TR(f)|^2 \cdot APSD(f)\,\mathrm{d}f} \tag{3.2}$$

Where $SDOF\_TR$ represents the transmissibility of the SDOF system and can be expressed as:

$$SDOF\_TR(f) = \frac{1 + 2i\xi(\frac{f}{f_n})}{1 - (\frac{f}{f_n})^2 + 2i\xi(\frac{f}{f_n})} \tag{3.3}$$

This method involves evaluating the integral for each natural frequency. Consequently, when the number of natural frequencies is high to achieve high accuracy, the computational cost will also be significant.

3.4.2. Lyapunov approach

Alternatively, there is another method to compute the acceleration RMS that is more computationally efficient. It is based on the Lyapunov equation, written as

$$\underline{\underline{\bar{A}}}\,\underline{\underline{\sigma^2_{\bar{x}\bar{x}}}} + \underline{\underline{\sigma^2_{\bar{x}\bar{x}}}}\,\underline{\underline{\bar{A}}}^T + \underline{\bar{B}} W \underline{\bar{B}}^T = \underline{0} \tag{3.4}$$

Here, $\underline{\underline{\bar{A}}}$ and $\underline{\bar{B}}$ are the state matrix and input matrix of the state space realization of the linear time-invariant system, respectively. W is the two-sided PSD of the white noise

input, and $\underline{\underline{\sigma^2_{\bar{x}\bar{x}}}}$ is the variance of the state, which is the unknown term of the equation. Solving the Lyapunov equation allows obtaining the variance of the state when the input is white noise. The variance of the output is then related to the variance of the state through Equation 3.5:

$$\sigma^2_{\bar{y}\bar{y}} = \underline{\bar{C}}\, \underline{\underline{\sigma^2_{\bar{x}\bar{x}}}}\, \underline{\bar{C}}^T \tag{3.5}$$

For the specific case under consideration:

$$\underline{\underline{\bar{A}}} = \begin{bmatrix} 0 & 1 \\ -\omega_n^2 & -2\xi\omega_n \end{bmatrix} \quad ; \quad \underline{\bar{B}} = \begin{bmatrix} 0 \\ -1 \end{bmatrix} \quad ; \quad \underline{\bar{C}} = \begin{bmatrix} -\omega_n^2 & -2\xi\omega_n \end{bmatrix} \tag{3.6}$$

The Lyapunov equation can be solved, resulting in:

$$\underline{\underline{\sigma^2_{xx}}} = \begin{bmatrix} \frac{W}{4\xi\omega_n^3} & 0 \\ 0 & \frac{W}{4\xi\omega_n} \end{bmatrix} \tag{3.7}$$

The variance of the output is then given by:

$$\sigma^2_{\bar{y}\bar{y}} = \frac{W 2\pi f}{4\xi}(1 + 4\xi^2) \tag{3.8}$$

This equation can be further expressed as:

$$\sigma^2_{\bar{y}\bar{y}} = \frac{W_0 \pi f}{4\xi}(1 + 4\xi^2) \tag{3.9}$$

Where W_0 represents the one-sided PSD associated with the white noise of the base acceleration. In the case of small damping, the equation can be approximated as:

$$\sigma^2_{\bar{y}\bar{y}} \approx \frac{W_0 \pi f}{4\xi} \tag{3.10}$$

This is commonly known as the Miles' equation.

In general, the acceleration in the input is not a white noise, and directly applying the Lyapunov equation may not be feasible. However, this problem can be addressed by introducing a shape filter in series with the linear time-invariant system. The purpose of this shape filter is to account for the non-constant acceleration PSD. It is crucial to

design the shape filter as a stable system to avoid introducing instability in the overall system and changing the dynamic of the system. The shape filter acts as an imaginary block, taking white noise as its input and producing the PSD of the base excitation as its output. A graphical representation can be found in Figure 3.3.

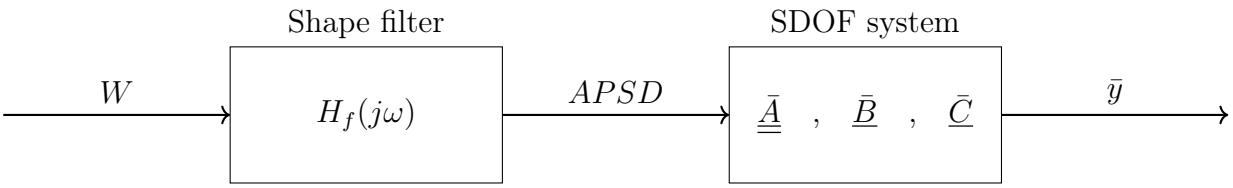

Figure 3.3: Block diagram: series connection between the shape filter and SDOF system.

Where $H_f(j\omega)$ represents the transfer function of the shape filter. The acceleration PSD in the output of the filter can be evaluated using the following formula:

$$APSD(\omega) = |H_f(j\omega)|^2 \, W \tag{3.11}$$

Assuming a unitary PSD of the white noise, the magnitude of the transfer function of the filter can be obtained as:

$$|H_f(j\omega)| = \sqrt{APSD(\omega)} \tag{3.12}$$

Once the transfer function of the filter is known, it allows us to derive the state space representation of the filter and, consequently, the augmented system. The state matrix and input matrix used in the Lyapunov equation correspond to those associated with the augmented system.

3.5. Case study and comparison between the methodologies

In this section, a comprehensive case study is presented, involving a meticulous comparison of two distinct methodologies. The focal point of this analysis revolves around the qualification levels commonly employed within the space industry for SC units. For reference, relevant data is included in Table 3.1.

Table 3.1: SC unit random qualification levels, sourced from [1].

			⊥ MOUNTING PLANE (OP)	
			RANGE (Hz)	LEVEL
m $\leq$ 50 kg	ON EXTERNAL PANELS	2.5 min duration	20 ÷ 100 100 ÷ 300 300 ÷ 2000	+3 dB/oct $0.12\frac{g^2}{Hz}\frac{m_{kg}+20kg}{m_{kg}+1kg}$ -5 dB/oct
			Global: to be calculated from the above APSD	
	ON INTERNAL PANELS	2.5 min duration	20 ÷ 100 100 ÷ 300 300 ÷ 2000	+3 dB/oct $0.05\frac{g^2}{Hz}\frac{m_{kg}+20kg}{m_{kg}+1kg}$ -5 dB/oct
			Global: to be calculated from the above APSD	
m > 50 kg	-	2.5 min duration	20 ÷ 110 110 ÷ 700 700 ÷ 2000	+3 dB/oct $0.09\ \frac{g^2}{Hz}$ -5 dB/oct
			Global: 11.14 gRMS	

Now, let's dissect the table itself. It provides a detailed breakdown of qualification levels based on the equipment's mass (m) and its location, whether it's positioned on external or internal panels. Furthermore, it specifies the duration of 2.5 minutes and the frequency range in Hz for each qualification level. Notably, it also presents the associated level values, showcasing the sensitivity of the equipment to vibrations with a slope represented as "+3 dB/oct" for the rising part and "-5 dB/oct" for the declining portion.

Moving forward, the case study involves placing equipment with a mass of 40 kg on an external panel. The equipment's vertical axis is assumed to be perpendicular to the mounting plane. Additionally, a 3-minute duration is considered for the analysis. This particular duration is a common industry practice, known for its conservative approach. These assumptions lead to the specification illustrated in Figure 3.4. Notably, within this specification, the flat value is identified as 0.1756 $\frac{g^2}{Hz}$.

The study proceeds with a thorough examination of the RMS, calculated using the classical methodology. Subsequently, this data is employed to compute the ERS. To validate these findings, a comparison is conducted against the ERS obtained using SinePost, a widely utilized software tool at Thales Alenia Space. The comparison results are graphically represented in Figure 3.5.

An interesting revelation emerges from this comparison: the ERS evaluated using the classical methodology aligns perfectly with the ERS derived from SinePost. This outcome

aligns with industry norms, as the classical methodology is the preferred approach within the space industry.

The case study undergoes an intriguing transformation as we delve into the evaluation of the ERS using the Lyapunov approach. The initial step entails constructing a shape filter, with filter coefficients obtained through the MATLAB function *invfreqs*. This function derives transfer function coefficients based on frequency response data. To complete the filter's characterization, both magnitude and phase information are essential, with the phase estimation relying on the Bode gain-phase relation (this process is further detailed in Appendix B.1).

The filter's order is determined through a trial and error approach, resulting in a 12^{th} order for the denominator and an 11^{th} order for the numerator. The resulting filter is expressed as the following transfer function.

$$\begin{aligned} H_f(s) = & \frac{(s+8064)(s+153.9)(s+2.149)}{(s+1.04e04)(s+1538)(s+560.5)(s+37.8)} \times \\ & \times \frac{(s^2+969s+3.041e06)(s^2+172.7s+6.82e07)}{(s^2+865.8s+3.18e06)(s^2+172.9s+6.82e07)} \times \\ & \times \frac{(s^2+91.53s+1.295e08)(s^2+3.059e04s+3.975e09)}{(s^2+91.57s+1.295e08)(s^2+1341s+2.945e09)} \end{aligned} \tag{3.13}$$

A comprehensive analysis comparing the square of the magnitude response of the filter to the APSD specification is depicted in Figure 3.6. This crucial comparison unveils the correspondence between the filter's behavior and the specific requirements outlined in the APSD specification.

Once the transfer function of the filter is determined, the next step involves constructing the state-space realization of the filter. Subsequently, this allows for the development of the state-space realization of the entire system, which includes the filter. With this augmented system in place, the Lyapunov equation is applied to derive essential insights. Specifically, the equation is employed to obtain the variance of the output acceleration, a fundamental metric in our analysis. The square root of this variance serves as the RMS value, which is a pivotal element required for evaluating the ERS.

To validate the results obtained through the Lyapunov approach, a comparative analysis against SinePost is carried out, and the results are visually presented in Figure 3.7. The curve derived using the Lyapunov approach demonstrates remarkable alignment with the benchmark solution. However, it's worth noting some minor deviations at 100 Hz and 300

Hz, primarily attributed to the filter's inherent limitations in accurately approximating the sharp variations present in the APSD specification.

Furthermore, substantial differences in the curve become apparent at the extremities, specifically around 20 Hz and after 1400 Hz. This deviation arises from SinePost's integral, which accounts for the finite domain of the Acceleration Power Spectral Density (APSD). This leads to distinct results in these frequency ranges, further demonstrated in Figure 3.8, which quantifies the relative error between the Lyapunov method and the SinePost solution.

Finally, the computational costs of the two methodologies are assessed. To provide a comprehensive view of the Lyapunov methodology's computational efficiency, the costs are broken down into three scenarios:

- Case A, where the filter and its state-space realization are assumed as given, and computational costs are evaluated solely for the loop over the natural frequencies.
- Case B, where the coefficients of the filter are considered as given, and the computational cost accounts for the loop over the natural frequencies of the SDOF system and the construction of the state-space realization of the filter.
- Case C, where the entire filter is treated as unknown, and the computational cost encompasses the loop over the natural frequencies of the SDOF system, along with the design of the filter, including phase estimation and coefficient estimation.

The results, summarized in Table 3.2, demonstrate that the Lyapunov method is more computationally efficient when looping over natural frequencies and when filter coefficients are known. However, it becomes slower than the classical methodology when accounting for the entire filter design process in the computational cost. Thus, the recommendation is to adopt the Lyapunov methodology if the specification and filter were already given, such as through a standard or a LVUM. This approach proves advantageous when evaluating and comparing numerous specifications, offering significant computational efficiency.

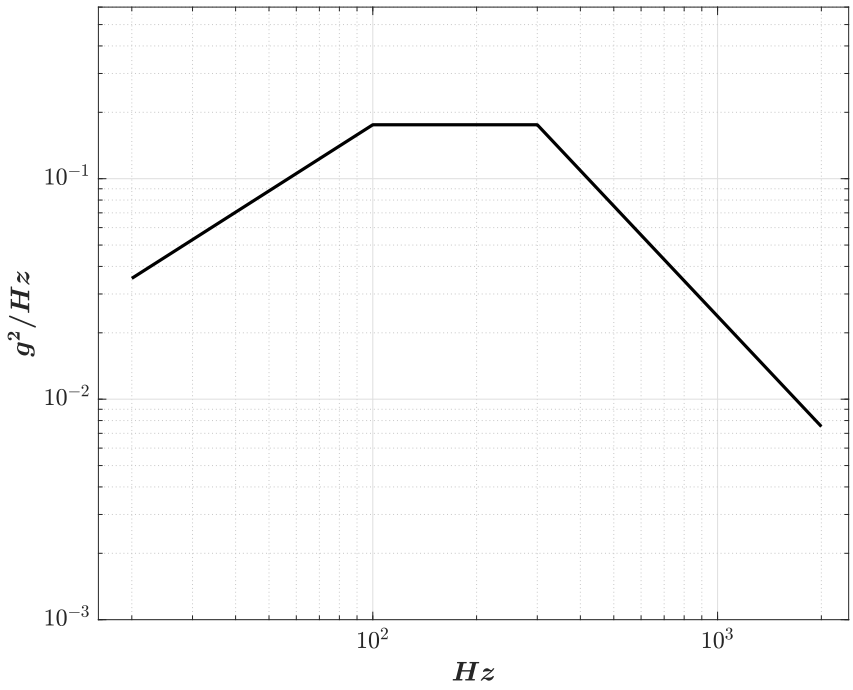

Figure 3.4: APSD specification.

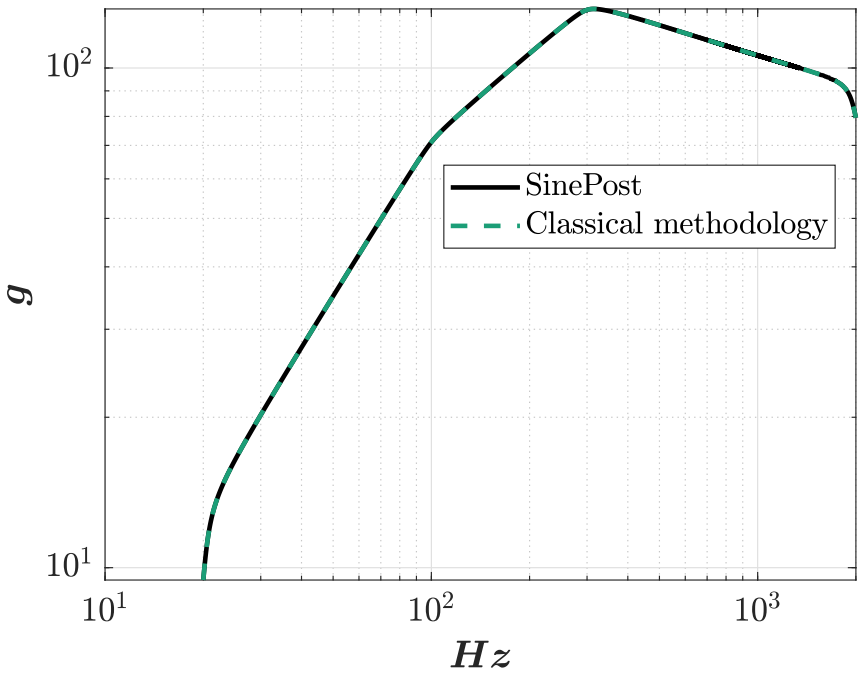

Figure 3.5: ERS: validation of the classical methodology against SinePost.

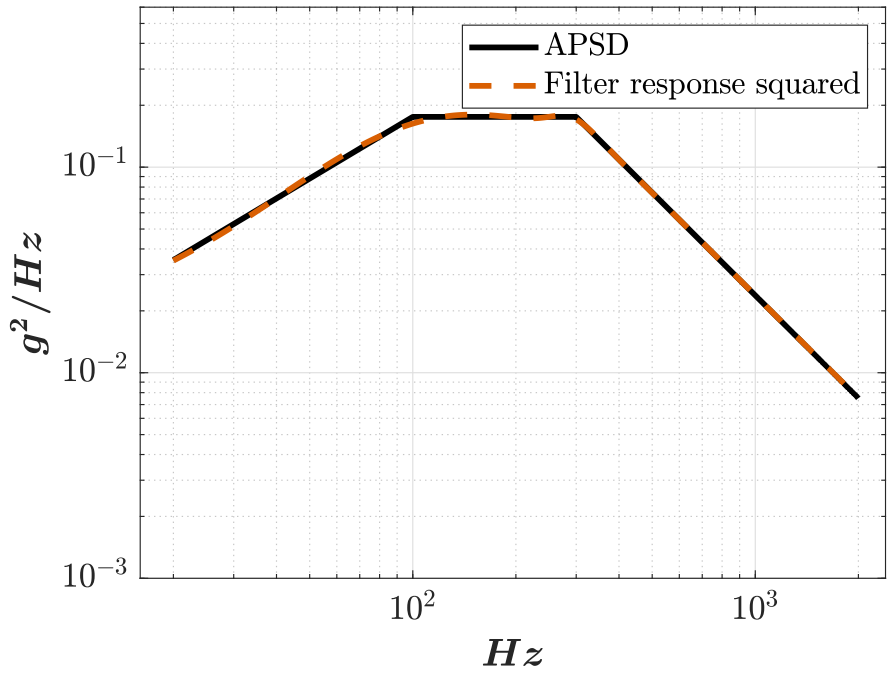

Figure 3.6: Comparison between the APSD and the filter response squared.

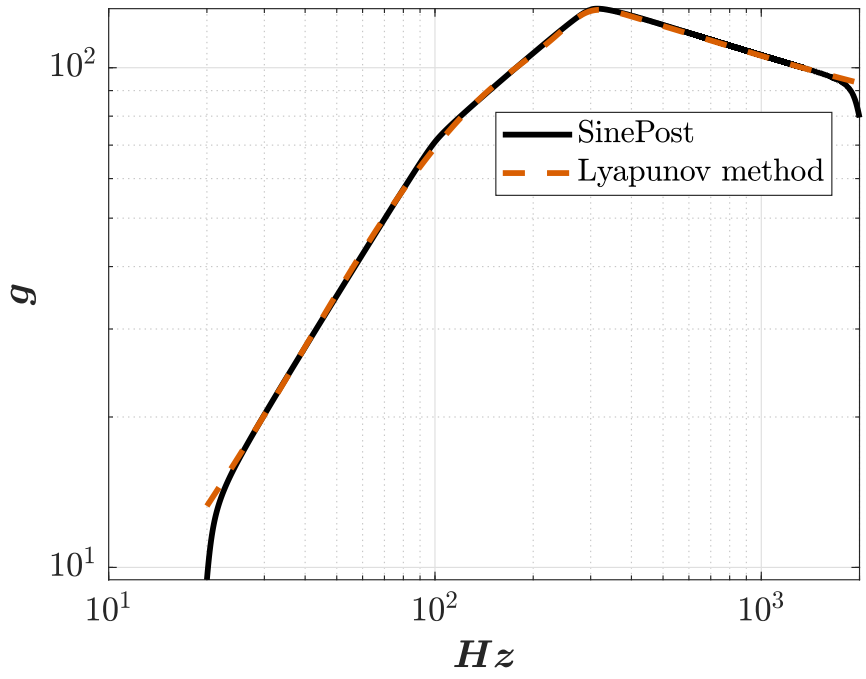

Figure 3.7: ERS: comparison of the Lyapunov methodology against SinePost.

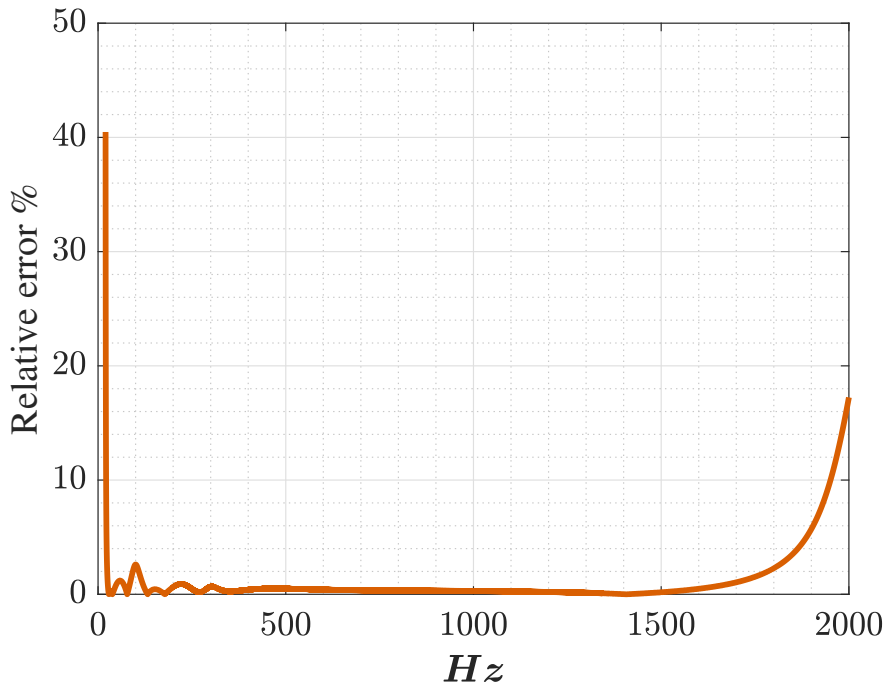

Figure 3.8: Relative error between the Lyapunov methodology and SinePost.

Table 3.2: Computational cost of the different methods, normalized with respect to the classical methodology.

Method	Computational Cost
Classical methodology	1
Case A	0.159
Case B	0.260
Case C	1.313

4 | Fatigue Damage Spectrum (FDS)

4.1. Overview

This chapter commences by providing an essential understanding of fatigue behavior in engineering, emphasizing its practical significance. It introduces the S-N curve, a pivotal concept in fatigue analysis. Furthermore, the chapter introduces the FDS as a vital metric for assessing the fatigue damage of structural components.

The chapter proceeds to explore two distinct methodologies for computing the FDS. It highlights that whether using random vibration data in the time domain or its PSD, both approaches yield identical results, a fact substantiated by McNeill [24].

Finally, the chapter conducts a comprehensive case study focusing on two APSD specifications. Here, the FDSs are computed by considering stress proportional to pseudo velocity (PV), relative displacement (RD), and absolute acceleration (AA). Importantly, the analysis reveals that the choice of approach for evaluating the FDS, for comparison purposes, does not significantly impact the resulting conclusions.

4.2. Fatigue behavior

Structures can compromise their integrity during service even when subjected to cyclic loading, even if stresses remain below the ultimate static strength. This phenomenon is known as fatigue.

When a mechanical system undergoes a high number of load cycles, it gradually diminishes its mechanical properties, including its strength. This can lead to structural failure occurring earlier than expected. The fatigue phenomenon is effectively captured by Whöler curves or S-N curves. An illustrative example of an S-N curve is provided in Figure 4.1, where S_a signifies the fixed maximum amplitude of the load, and N denotes the number of cycles until failure. The Basquin law, expressed as $S_a^{\alpha} N = const$, is employed to

characterize fatigue behavior, where α is dependent on the material's properties. In the aerospace realm, both planes and military aircraft experience load cycles during activities such as taxiing and ground-air-ground maneuvers. Similarly, SC are subjected to load cycles during transportation, shaker testing, and while within the LV.

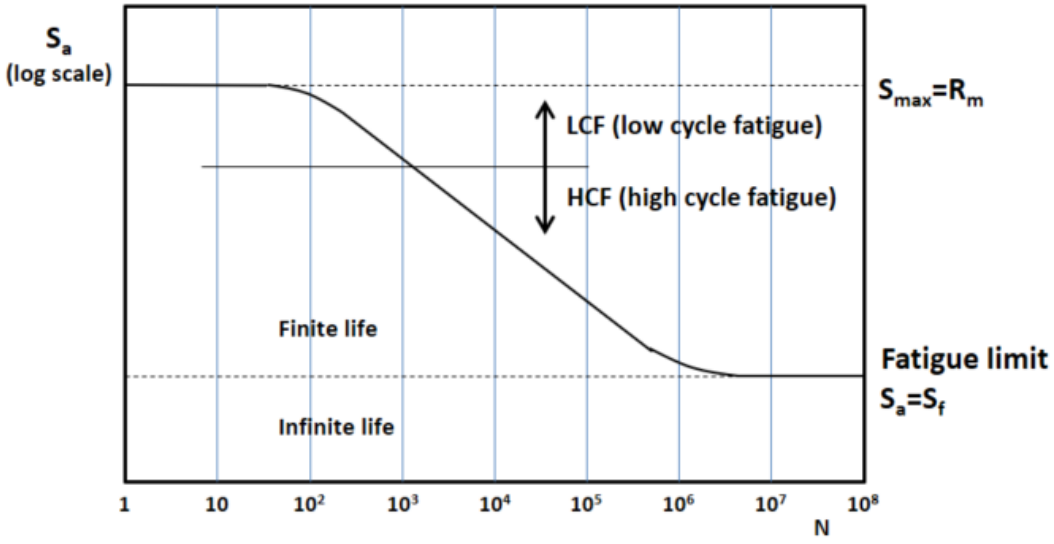

Figure 4.1: Example of an S-N curve.

While SRS and ERS are valuable tools for assessing a structure's peak response to shocks or mechanical vibrations, they lack insights into the resulting structural damage. The FDS, an extension of the ERS, quantifies fatigue damage based on the SDOF system's frequency. This framework enables the comparison of APSD specifications with varying durations. The FDS has proven useful in appraising the fatigue potential of different shakers, as demonstrated in the work by Henderson [16], and in contrasting existing specifications with new ones.

4.3. How to compute the FDS

The assessment of the FDS varies depending on whether the acceleration is presented as a time history or represented via its PSD. In either scenario, akin to the approach used for SRS and ERS, the acceleration is imposed at the base of an array of SDOF systems. The provided formulation accounts for stress in each SDOF system, and this stress is proportionate to the PV, as indicated by the researches conducted by Hunt and Gaberson [14, 17]. However, in alternative studies, stress has been approached in different ways. For instance, Lalanne [23] has considered stress as proportional to RD, while Di

Maggio [12] has linked stress to AA.

4.3.1. Base acceleration expressed as a time history

When the base acceleration is provided as a time history, the process of assessing the FDS can be condensed into three essential steps:

1. **Calculation of PV**: Begin by calculating the PV for each individual SDOF system.
2. **Cycle Counting**: Utilize a dedicated counting cycle algorithm to quantify the occurrence of cycles.
3. **Damage Computation**: Apply the Basquin law and the Palmgreen-Miner rule to compute the extent of damage.

The PV of a SDOF system is determined using a filtering technique, similar to the one employed for SRS. This technique utilizes a recursive formula, sourced from McNeill [24], which is provided below:

$$pv(k) = b_0\,a(k) + b_1\,a(k-1) + b_2\,a(k-2) - a_1\,pv(k-1) - a_2\,pv(k-2) \tag{4.1}$$

The coefficients required for this computation can be found in Appendix C.1.

Once the PV is known as a function of time, cycle counting can be conducted. A prevalent method for this purpose is the Rainflow cycle counting, which is elaborated in [7].

Damage assessment is achieved using the Palmgreen-Miner rule, as depicted in Equation 4.2:

$$D = \sum_i \frac{n_i}{N_i} \tag{4.2}$$

Here, n_i represents the measured cycles with stress amplitude S_i, and N_i is the number of cycles with stress amplitude S_i causing failure. By leveraging the Basquin law, one can deduce $N_i = c\,S_i^{-b}$. Substituting this into the Palmgreen-Miner rule yields the damage expression:

$$D = \frac{k^\alpha}{c} \sum_i n_i\,PV_i^b \tag{4.3}$$

In this equation, S_i is replaced with kPV_i, where k is a constant of proportionality.

4.3.2. Base acceleration expressed through its PSD

When the base acceleration is expressed in terms of its PSD, the estimation of fatigue damage can be conducted using Equation 4.4, as referenced from [16, 24].

$$D = \frac{f_n T}{c} k^{\alpha} \left[\sqrt{2}\sigma_{pv}\right]^{\alpha} \Gamma\left(1 + \frac{\alpha}{2}\right) \tag{4.4}$$

In this equation, Γ signifies the gamma function, where $\Gamma(x) = (x-1)!$, and σ_{pv} denotes the RMS of the PV.

To compute the RMS of the PV, the integral Equation 3.2 can be employed. However, this time, instead of utilizing the transmissibility which establishes the connection between the output acceleration and the input acceleration, the *PV Transmissibility* should be used, denoted as $SDOF\_PV\_TR$, representing the relationship between the output PV and the input AA.

To derive this relationship, the transmissibility in Equation 3.3 can be manipulated. Begin by subtracting 1. Then, multiply by $-\frac{1}{\omega^2}$ to acquire the relationship between the output RD and the input AA. This resultant relationship, termed *RD Transmissibility*, noted as $SDOF\_RD\_TR$, can be expressed as:

$$SDOF\_RD\_TR(f) = \frac{(\frac{f}{f_n})^2}{1 + 2i\xi\frac{f}{f_n} - (\frac{f}{f_n})^2} \cdot (-\frac{1}{w^2}) \tag{4.5}$$

By multiplying the expression 4.5 by w_n, the relationship between the output PV and the input AA can be derived, termed the *PV Transmissibility*, denoted as $SDOF\_PV\_TR(f)$:

$$SDOF\_PV\_TR(f) = -\frac{\frac{1}{2\pi f_n}}{1 + 2i\xi\frac{f}{f_n} - (\frac{f}{f_n})^2} \tag{4.6}$$

The RMS can alternatively be determined by utilizing the Lyapunov approach elaborated upon in Section 3.4. Subsequent to evaluating the RMS, it can be inserted into Equation 4.4 to derive the cumulative damage. Modifying σ_{pv} with the RMS of another parameter, such as AA or RD, will result in the consideration of stress proportionality with those specific quantities.

4.4. Case study and comparison

The provided data for the case study are sourced from Irvine [19]. Let's consider a component that has undergone testing with a specific specification A. Now, a new specification B is introduced, and the goal is to ascertain whether the component needs to be tested anew with the new specification. The details of specifications A and B are outlined in Tables 4.1 and 4.2, respectively. An illustrative representation of both specifications is depicted in Figure 4.2.

Table 4.1: Specification A PSD.

Frequency $[Hz]$	**APSD $[g^2/Hz]$**
15	0.04
47.26	0.159
300	0.260
1000	1.313
2000	0.118
Global: 25 gRMS, 1 hour/axis	

Table 4.2: Specification B PSD.

Frequency $[Hz]$	**APSD $[g^2/Hz]$**
10	0.04
40	0.04
2000	0.006
Global: 4.6 gRMS, 5 hours/axis	

Upon analyzing the graphical representation of both specifications, it's evident that $APSDA \geq APSDB$. It might seem that the severity of A is consistently greater than or equal to the severity of B, possibly indicating that retesting isn't necessary.

To comprehensively compare the severities of the two specifications, the analysis is conducted under three cases:

i Stress proportional to PV

ii Stress proportional to AA

iii Stress proportional to RD

The corresponding graph depicting these three cases can be observed in Figure 4.3. The observed trend reveals that, across all three cases, the severities of the two specifications intersect. This suggests that the component should indeed be subjected to testing with the new specification (B). This phenomenon can be explained by recognizing that APSD is a density measure, and as such, it shouldn't be employed for direct comparison between different loads. Furthermore, it's noteworthy that the crossing frequency appears similar across the three cases.

It's important to clarify that while the crossing frequency seems the same, it's not precisely so. Specifically, the crossing frequency for stress proportional to PV and RD is 71.6 Hz, while for stress proportional to AA, it's 71.5 Hz. This discrepancy can be understood in light of the fact that PV and RD both pertain to the relative motion of the SDOF, whereas AA relates to the AA of the mass. The proximity of the crossing frequency in the AA case to the other cases can be attributed to the relatively much greater magnitude of the mass's response compared to the base motion, which is assumed negligible.

In summary, the choice of approach for evaluating the FDS for comparison purposes doesn't significantly impact the conclusions drawn, as they all lead to the same conclusion. This is substantiated in studies like Grillo [15] and Minderhoud [25], which demonstrate that different approaches yield consistent results when synthesizing the specification using FDS.

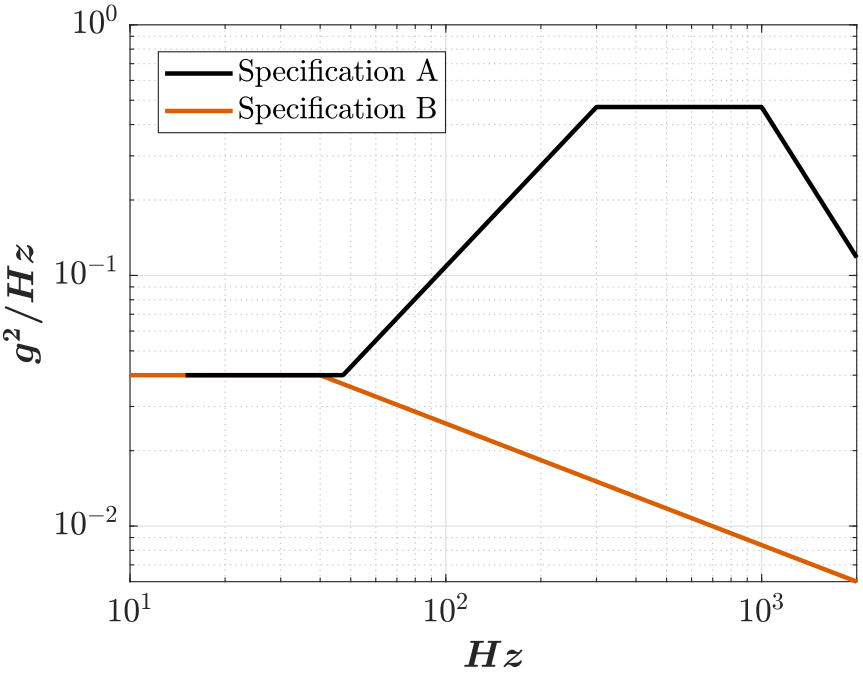

Figure 4.2: PSD specifications.

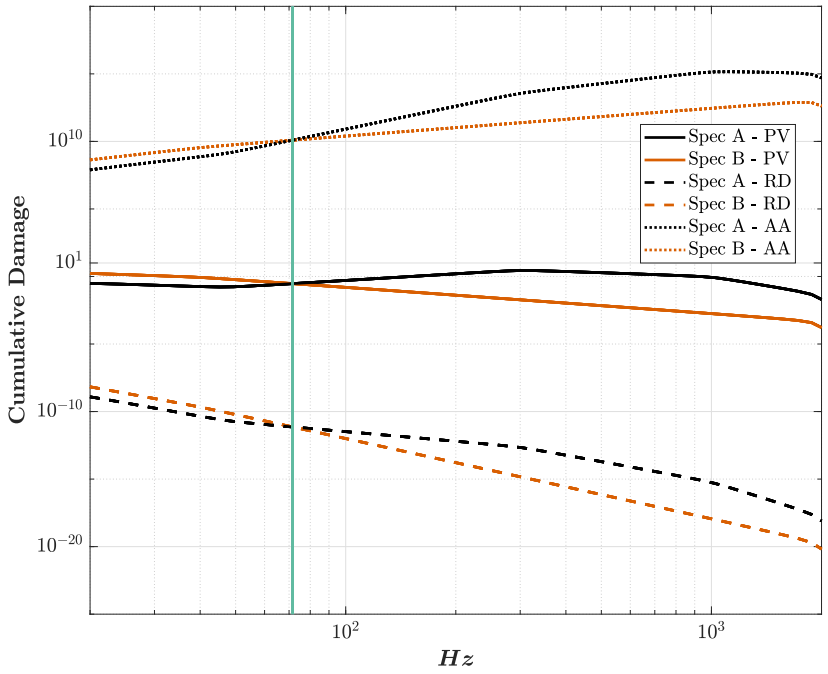

Figure 4.3: Comparison of the comparison between FDS evaluated considering the stress proportional to PV, RD and AA.

5 | Proposed 6DOF approach for mechanical severity comparison

5.1. Overview

This chapter delves into the crucial concept of assessing mechanical severity in scenarios involving 6DOF enforced accelerations. The narrative begins by elucidating the necessity of adopting a 6DOF approach when calculating and comparing severities arising from different loads. This approach extends beyond the simplified SDOF framework, providing a more comprehensive perspective.

The journey commences with the development of a novel criterion explicitly designed for 6DOF systems. This criterion hinges on the forces at the IF and their pivotal role in characterizing the severity of 6DOF enforced accelerations. It recognizes that, unlike SDOF cases, 6DOF systems demand a more intricate framework that accounts for both translational and rotational dynamics.

In the subsequent section, the intricacies of evaluating IF forces are explored. This process is pivotal for understanding how forces manifest in 6DOF systems and their contribution to overall mechanical severity. Various methodologies and techniques are presented to enable a robust assessment of forces at the interface.

To solidify the concepts introduced in this chapter, a comprehensive case study involving a SC mounted on a LV is presented. This real-world scenario embodies the complexities of 6DOF systems subjected to dynamic loading conditions. The force-based approach for mechanical severity comparison is showcased, demonstrating its practical applicability.

In the final segment of this chapter, the force-based approach is validated by comparing it against results obtained from a Finite Element (FE) analysis performed with MSC Nastran. This validation process ensures the reliability and accuracy of the proposed methodology in practical engineering scenarios.

5.2. Need of a 6DOF approach

As previously discussed in Section 2.6, structural qualification dynamic tests for the low-frequency range are typically conducted on monoaxial shakers, with each axis tested individually using a sine sweep. However, real-life operational loads are often multiaxial in nature. Take, for instance, the load at the LV-SC IF, which exhibits multiaxial characteristics. When qualification tests are performed on monoaxial shakers, they tend to employ significantly more conservative qualification levels for each axis compared to the severity calculated from the actual operative load projected along that same axis. This conservative approach compensates for the fact that the testing is conducted one axis at a time.

While a 6DOF shaker could theoretically replicate the 6DOF qualification profile by applying a Qualification Factor of Safety (FoS) to the operative load profile, practical limitations prevent exact replication. Consequently, a method is required to evaluate the severities of both the qualification profile and the operative load profile. Additionally, a criterion for comparison is needed to ensure that the qualification load's severity exceeds that associated with the operative load.

The existing criterion states that if the severity of load A is greater than that of load B, the risk of structural failure when subjected to load A is higher. However, it's important to note that this criterion primarily relies on SDOF systems for evaluating load severity. This criterion is particularly effective when the internal structural mode shapes exhibit minimal coupling. In simpler terms, it works best when the modal frequencies of the entire structure and its individual sub-components do not closely coincide.

5.3. Criterion for comparing different severities

In the realm of vibration analysis, comparing different severities is a fundamental aspect of assessing structural responses. Traditionally, in the SDOF scenario, the severity of a base-enforced acceleration is quantified by the maximum absolute acceleration experienced by the SDOF system's mass. This acceleration effectively represents the internal forces acting on the system.

However, the situation becomes more intricate when transitioning to the context of 6DOF systems. In this scenario, the absolute acceleration can accurately represent translational forces but falls short in capturing moments since these depend on the structure's inertia. Consequently, when evaluating the severity of a 6DOF enforced acceleration, the rigid body mass matrix comes into play. The traditional criterion for severity comparison must

be reformulated to account for these nuanced considerations, emphasizing the forces at the IF rather than the absolute acceleration of the mass.

To formulate an appropriate criterion, two distinct cases are proposed. First, scenarios where base rotational accelerations can be considered negligible compared to translational ones are examined. In such cases, the criterion can be expressed as follows:

For two 3DOF base-enforced translational accelerations, denoted as A and B, the mechanical severity of A surpasses that of B if the following conditions are met:

$$|F_x^A(\bar{f})|_{max} > |F_x^B(\bar{f})|_{max} \tag{5.1}$$
$$|F_y^A(\bar{f})|_{max} > |F_y^B(\bar{f})|_{max} \tag{5.2}$$
$$|F_z^A(\bar{f})|_{max} > |F_z^B(\bar{f})|_{max} \tag{5.3}$$

Here, F represents the forces at the interface, and $\bar{f}$ denotes the frequencies considered.

This criterion reveals an interesting analogy to the SDOF severity criterion. In situations where rotations at the base are negligible, it's akin to considering an SDOF system for each of the three translational directions. In such cases, the criterion can potentially be formulated in terms of accelerations instead of forces, with the mass acting as the only scaling factor.

Conversely, when rotations at the base are not negligible, and the base-enforced acceleration exhibits 6DOFs, the criterion evolves to accommodate these complexities. For two 6DOF base-enforced translational accelerations, A and B, the mechanical severity of A outweighs that of B if the following conditions are met:

$$|F_x^A(\underline{f})|_{max} > |F_x^B(\underline{f})|_{max} \tag{5.4}$$
$$|F_y^A(\underline{f})|_{max} > |F_y^B(\underline{f})|_{max} \tag{5.5}$$
$$|F_z^A(\underline{f})|_{max} > |F_z^B(\underline{f})|_{max} \tag{5.6}$$
$$|M_x^A(\underline{f})|_{max} > |M_x^B(\underline{f})|_{max} \tag{5.7}$$
$$|M_y^A(\underline{f})|_{max} > |M_y^B(\underline{f})|_{max} \tag{5.8}$$
$$|M_z^A(\underline{f})|_{max} > |M_z^B(\underline{f})|_{max} \tag{5.9}$$

Once again, F and M represent the forces and the moments at the interface, respectively; instead $\underline{f}$ indicates the vector of the first natural frequencies for each DOF of the system.

Further customizations of the above conditions could be put in place in specific cases,

for example comparing separately the maximum and the minimum values instead of considering the absolute ones, which could be useful to be consistent with respect to some buckling phenomena or, more broadly, to account for nonlinearities.

This refined criterion accounts for the multidimensional nature of 6DOF base-enforced accelerations, offering a robust framework for assessing and comparing structural severities in complex vibration scenarios.

5.4. Formulation of the approach

Consider a mass that can freely rotate and translate, exhibiting 6 degrees of freedom, encompassing three translational and three rotational movements. The governing equation for this system, known as the Rigid Body Motion (RBM) equation, is expressed as:

$$\underline{F}_{IN} = \underline{\underline{M}}\,\underline{\ddot{u}} \tag{5.10}$$

In this equation, $\underline{F}_{IN}$ represents the vector of inertial forces and moments, $\underline{\underline{M}}$ denotes the mass matrix, and $\underline{\ddot{u}}$ signifies the acceleration vector.

Expanding Equation 5.10 reveals:

$$\begin{Bmatrix} F_x \\ F_y \\ F_z \\ M_x \\ M_y \\ M_z \end{Bmatrix}_{IN} = \begin{bmatrix} m & 0 & 0 & 0 & mg_z & -mg_y \\ 0 & m & 0 & -mg_z & 0 & mg_x \\ 0 & 0 & m & mg_y & -mg_x & 0 \\ 0 & -mg_z & mg_y & I_{xx} & -I_{xy} & -I_{xz} \\ mg_z & 0 & -mg_x & -I_{xy} & I_{yy} & -I_{yz} \\ -mg_y & mg_x & 0 & -I_{xz} & -I_{yz} & I_{zz} \end{bmatrix} = \begin{Bmatrix} \ddot{x} \\ \ddot{y} \\ \ddot{z} \\ \ddot{\theta} \\ \ddot{\phi} \\ \ddot{\psi} \end{Bmatrix} \tag{5.11}$$

Here, m represents the mass of the structure, while g_i denotes the coordinates of the center of mass of the structure with respect to the base IF, and I_{ij} signifies the moments of inertia of the structure concerning the base IF. The rotations around the x, y, and z axes are represented as θ, ϕ, and ψ, respectively.

This mass is connected to a base through 6 springs and 6 dampers, each corresponding to a DOF. The forces pertaining to elasticity and damping concerning a fixed base can be defined as:

$$\underline{F}_{EL} = \underline{\underline{K}}\,\underline{u} \tag{5.12}$$

Or, in an expanded form:

$$\begin{Bmatrix} F_x \\ F_y \\ F_z \\ M_x \\ M_y \\ M_z \end{Bmatrix}_{EL} = \begin{bmatrix} k_{xx} & 0 & 0 & 0 & 0 & 0 \\ 0 & k_{yy} & 0 & 0 & 0 & 0 \\ 0 & 0 & k_{zz} & 0 & 0 & 0 \\ 0 & 0 & 0 & k_{\theta\theta} & 0 & 0 \\ 0 & 0 & 0 & 0 & k_{\phi\phi} & 0 \\ 0 & 0 & 0 & 0 & 0 & k_{\psi\psi} \end{bmatrix} = \begin{Bmatrix} x \\ y \\ z \\ \theta \\ \phi \\ \psi \end{Bmatrix} \tag{5.13}$$

and

$$\underline{F}_{DMP} = \underline{\underline{C}}\,\underline{\dot{u}} \tag{5.14}$$

or in an expanded form:

$$\begin{Bmatrix} F_x \\ F_y \\ F_z \\ M_x \\ M_y \\ M_z \end{Bmatrix}_{DMP} = \begin{bmatrix} c_{xx} & c_{xy} & c_{xz} & c_{x\theta} & c_{x\phi} & c_{x\psi} \\ c_{yx} & c_{yy} & c_{yz} & c_{y\theta} & c_{y\phi} & c_{y\psi} \\ c_{zx} & c_{zy} & c_{zz} & c_{z\theta} & c_{z\phi} & c_{z\psi} \\ c_{\theta x} & c_{\theta y} & c_{\theta z} & c_{\theta\theta} & c_{\theta\phi} & c_{\theta\psi} \\ c_{\phi x} & c_{\phi y} & c_{\phi z} & c_{\phi\theta} & c_{\phi\phi} & c_{\phi\psi} \\ c_{\psi x} & c_{\psi y} & c_{\psi z} & c_{\psi\theta} & c_{\psi\phi} & c_{\psi\psi} \end{bmatrix} = \begin{Bmatrix} \dot{x} \\ \dot{y} \\ \dot{z} \\ \dot{\theta} \\ \dot{\phi} \\ \dot{\psi} \end{Bmatrix} \tag{5.15}$$

The equation of motion for the entire system can be expressed as:

$$\underline{\underline{M}}\,\underline{\ddot{u}} + \underline{\underline{C}}\,\underline{\dot{r}} + \underline{\underline{K}}\,\underline{r} = \underline{0} \tag{5.16}$$

Here, $\underline{r} = \underline{u} - \underline{b}$ represents the relative displacement between the mass and the base. This equation can be reformulated as follows:

$$\underline{\underline{M}}\,\underline{\ddot{r}} + \underline{\underline{C}}\,\underline{\dot{r}} + \underline{\underline{K}}\,\underline{r} = -\underline{\underline{M}}\,\underline{b} \tag{5.17}$$

To solve this equation, the modal approach can be employed. Assuming small damping, the natural frequencies and mode shapes of the mass structure can be obtained by solving the following eigenvalue problem:

$$\left(\underline{\underline{K}} - \omega_i^2 \underline{\underline{M}}\right) \underline{R}_i = \underline{0} \tag{5.18}$$

Once the eigenvector matrix $\underline{\underline{R}}$ is available, the displacement vector can be expressed as $\underline{r} = \underline{\underline{R}}\,\underline{r}_g$, where $\underline{r}_g$ represents the vector of generalized displacements. Substituting this expression into Equation 5.17, we derive:

$$\underline{\underline{M}}\,\underline{\underline{R}}\,\ddot{\underline{r}}_g + \underline{\underline{C}}\,\underline{\underline{R}}\,\dot{\underline{r}}_g + \underline{\underline{K}}\,\underline{\underline{R}}\,\underline{r}_g = -\underline{\underline{M}}\,\underline{b} \tag{5.19}$$

By projecting this equation onto the modal space with a premultiplication by $\underline{\underline{R}}_g^T$, we obtain:

$$\underline{\underline{M}}_g\,\ddot{\underline{r}}_g + \underline{\underline{C}}_g\,\dot{\underline{r}}_g + \underline{\underline{K}}_g\,\underline{r}_g = -\underline{\underline{R}}^T\,\underline{\underline{M}}\,\underline{b} \tag{5.20}$$

In this equation, $\underline{\underline{M}}_g = \underline{\underline{R}}^T\,\underline{\underline{M}}\,\underline{\underline{R}}$, $\underline{\underline{C}}_g = \underline{\underline{R}}^T\,\underline{\underline{C}}\,\underline{\underline{R}}$, and $\underline{\underline{K}}_g = \underline{\underline{R}}^T\,\underline{\underline{K}}\,\underline{\underline{R}}$. Due to the orthogonality property of $\underline{\underline{R}}$, matrices $\underline{\underline{M}}_g$, $\underline{\underline{C}}_g$, and $\underline{\underline{K}}_g$ are diagonal, leading to a decoupled system. The state-space form of the system can be written similarly to Subsection 2.7.1, and it can be solved using the MATLAB function *lsim*.

Once $\underline{r}_g$ and $\dot{\underline{r}}_g$ are obtained, $\underline{r}$ and $\dot{\underline{r}}$ can be found using the eigenvectors matrix $\underline{\underline{R}}$, and the force at the base IF can be computed as follows:

$$\underline{F}_{IF} = \underline{\underline{K}}\,\underline{r} + \underline{\underline{C}}\,\dot{\underline{r}} \tag{5.21}$$

Matrices $\underline{\underline{K}}$ and $\underline{\underline{M}}$ are required to solve the generalized eigenvalue problem. $\underline{\underline{M}}$ can be extracted from the 3D model of the SC, while an approach for obtaining $\underline{\underline{K}}$ is presented here. A FE modal analysis can be performed to determine the first natural frequency of the SC for each degree of freedom. These frequencies can be used to compute an initial guess for the diagonal values of the matrix $\underline{\underline{K}}$, which can be obtained through Equation 5.22:

$$\underline{k}_{guess} = \mathrm{diag}(\underline{\underline{M}}) \odot (2\pi \underline{f})^2 \tag{5.22}$$

In this equation, $\underline{k}_{guess}$ represents the initial guess vector for the diagonal of $\underline{\underline{K}}$, and $\underline{f}$ is the vector containing the natural frequencies obtained from the FE modal analysis. Subsequently, the eigenvalue problem can be solved to obtain the natural frequencies

and mode shapes for all 6 DOFs. The sum of the squares of the differences between the obtained natural frequencies and the known ones can be minimized using the MATLAB function *lsqnonlin*.

5.5. Approximation made and applicability domain of the approach

The approach illustrated in Section 5.3 aims at approximating the base IF forces and moments occurring in case of MDOF enforced dynamic excitation to the base of the structure. The solution is found by referring to a fictitious system having only six main global modes (three translational and three rotational), considered with the corresponding damping. Moreover, the rigid body mass matrix is directly used as the relation between base acceleration and rotations and IF forces and moments. The above fictitious system provides a simplified approximation of the global behavior of the real one and, as such, should not be suitable to estimate the magnitude of the structure base IF forces and moments. Conversely, it can be more reliable in order to perform the severity comparison of different MDOF IF loads, just in terms of relative quantities. For example, this comes to be quite useful when assessing if a shaker MDOF qualification test run is more severe than the expected maximal operative loads, considered with appropriate margins. The advantages of the proposed methodology is that no dedicated transient dynamic analysis involving the entire structure is required to make the MDOF severity comparison, while only its rigid body mass matrix and the main six natural frequencies are required. The same approach could be exploited to MDOF random and fatigue damage domains.

5.6. Case study and comparative analysis: MATLAB vs. MSC Nastran

To validate the approach and explore its real-world implications, a MATLAB code was implemented for evaluating the severities of a 6DOF base-enforced acceleration and comparing them, following the methodology outlined in Section 5.5.

The case study revolves around a SC mounted on a LV, with the load at the SC base transmitted through an adapter. The provided rigid body mass matrix is as follows:

$$\underline{\underline{M}} = \begin{bmatrix} 9.787\text{e+}02 & 2.193\text{e}-17 & -3.375\text{e}-17 & -6.904\text{e}-17 & 9.120\text{e+}02 & -7.788\text{e}-01 \\ 2.193\text{e}-17 & 9.787\text{e+}02 & -1.862\text{e}-16 & -9.120\text{e+}02 & 4.863\text{e}-16 & 9.825\text{e+}00 \\ -3.375\text{e}-17 & -1.862\text{e}-16 & 9.787\text{e+}02 & 7.788\text{e}-01 & -9.825\text{e+}00 & -1.048\text{e}-16 \\ -6.904\text{e}-17 & -9.120\text{e+}02 & 7.788\text{e}-01 & 1.792\text{e+}03 & -1.835\text{e+}01 & -3.993\text{e+}00 \\ 9.120\text{e+}02 & 4.863\text{e}-16 & -9.825\text{e+}00 & -1.835\text{e+}01 & 1.785\text{e+}03 & -3.674\text{e+}00 \\ -7.788\text{e}-01 & 9.825\text{e+}00 & -1.048\text{e}-16 & -3.993\text{e+}00 & -3.674\text{e+}00 & 6.834\text{e+}02 \end{bmatrix} \tag{5.23}$$

To calculate the first natural frequencies for each DOF, a FE modal analysis was performed. These frequencies were organized as:

$$f_{FEM} = \begin{Bmatrix} 1\text{e+}05 & 1\text{e+}05 & 63.791 & 22.889 & 22.726 & 54.614 \end{Bmatrix}^T \tag{5.24}$$

These frequencies corresponded to DOFs ordered as $\begin{Bmatrix} x & y & z & \theta & \phi & \psi \end{Bmatrix}$. Notably, f_x and f_y were set to 1e+05 due to the stiff connection between the SC and the adapter through an *RBE2* element.

The base-enforced acceleration for the study was derived from a LV-SC CLA. Two key scenarios were considered:

1. **3DOF Case**: Only the translational components of the base acceleration were considered, representing tests performed with shakers on one axis at a time.
2. **6DOF Case**: All components of the base acceleration were considered, representing a comprehensive scenario similar to a full CLA.

In both cases, the forces and moments at the IF were evaluated using both MATLAB and a FE analysis performed in MSC Nastran.

Figure 5.1 presents the results obtained from the analyses, focusing on F_z, M_x and M_y as they represent the most significant and severe loading conditions. In both analyses, it was observed that the forces at the IF for the 3DOF case exceeded those for the 6DOF case. This finding indicates that when conducting SC tests on a shaker axis by axis, the severity of the load is not representative of the true 6DOF scenario. Consequently, the SC may be subjected to overtesting. In this example, this does not hold true for the force F_z because its characteristics are unique, stemming from the structure's rigid body mass matrix. The associated terms for other translations and rotations are several orders of magnitude lower than that for translation in the z direction.

The validation of the force severity approach is critical. While the results for F_z and M_x align closely with those obtained from MSC Nastran, there is a notable discrepancy in the case of M_y. This discrepancy can be attributed to the underlying assumptions of the MATLAB-based force severity approach. In this approach, the dynamics of the SC are approximated, as discussed in Subsection 5.5, using only the first natural frequency in each axis. In contrast, by inspecting the MSC Nastran analysis, it is evident that the T_x component of the enforced acceleration, responsible for exciting M_y, has a frequency that corresponds to the second mode, which is at approximately $40, \mathrm{Hz}$.

The severity comparison is performed through the ratio between the force or moment calculated for the load case 1 and the force or moment calculated for the load case 2. As a criterion, positive and negative values are treated separately and the maximum of the two ratios is thus retained. In Figure 5.2, each bar provides the result of the severity comparison performed. It becomes evident that the force severity comparison approach provides a good approximation of the real severity comparison. Consequently, the force severity approach serves as a valuable tool for comparing different severities, as the result of the comparison does not depend on the magnitude of the forces at the IF. Additionally, it offers the advantage of not necessitating a full transient FE analysis, as it only requires the SC's rigid body mass matrix and its first natural frequencies.

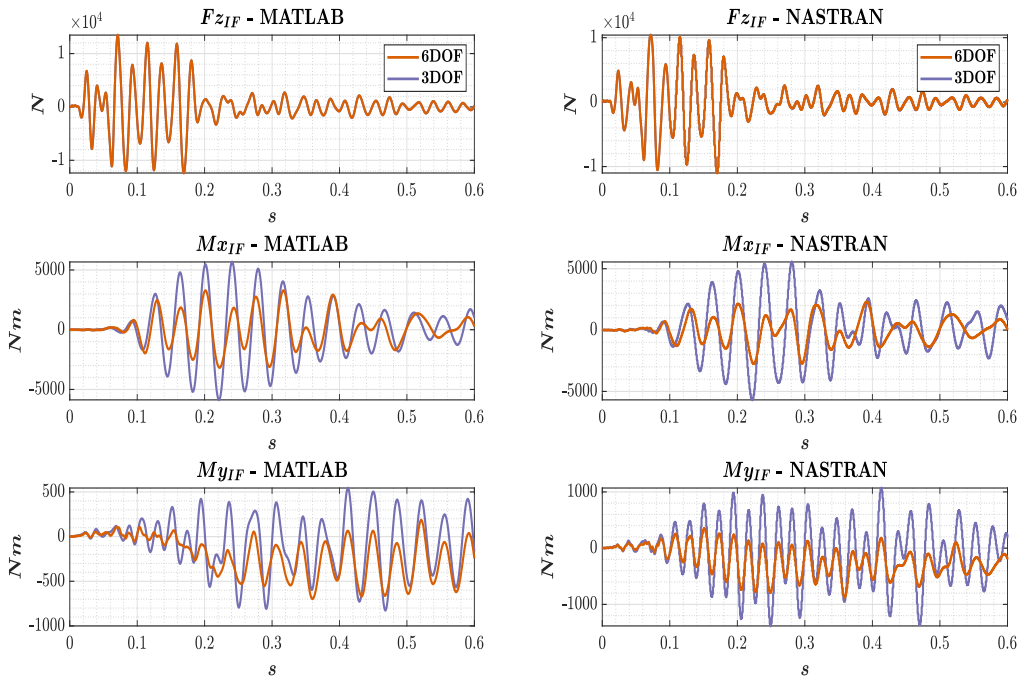

Figure 5.1: IF forces for the 3DOF and 6DOF cases evaluated through MATLAB and MSC Nastran.

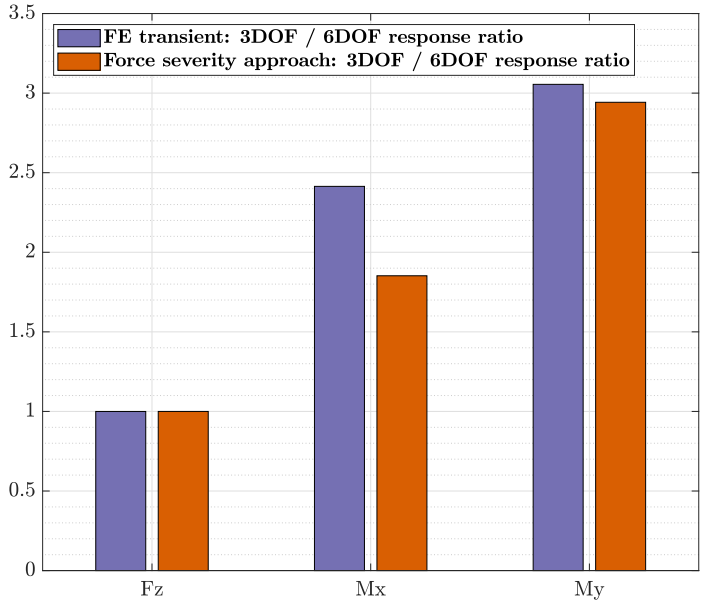

Figure 5.2: Histogram representing the largest ratios of the IF forces for the 3DOF and 6DOF cases.

6 | Conclusions and future developments

In the course of this thesis, various facets of prevailing methodologies for assessing and contrasting diverse mechanical load severities have undergone thorough examination, leading to the proposal of several enhancements.

For the ERS, a convenient approach for evaluating the root mean square has been introduced. This alternative methodology has the potential to reduce computational costs in certain scenarios, making it a promising addition to the toolbox of severity assessment techniques.

Regarding the FDS, an essential observation emerged. The evaluation of the FDS for comparison purposes is fundamentally independent of the specific stress quantity chosen for proportionality. This insight highlights the versatility and robustness of the FDS, underlining its utility in assessing fatigue-related severities across various contexts.

The most compelling findings, however, center around the SRS. In-depth exploration of a 2DOF system, as detailed in Section 2.7, has demonstrated a critical limitation in the prevailing metrics for evaluating the severity of mechanical loads in terms of local accelerations of the structures considered. These metrics, primarily founded on the responses of SDOF systems, tend to lose accuracy as systems grow more complex. This finding, coupled with the expanding body of research on 6DOF shakers, provides a compelling rationale for a more rigorous and consistent discussion about the limitations of the mechanical load severity (which should not be intended independently of the structure) and give the reason for the development of a more precise methodology for mechanical severity comparison, as delineated in Chapter 5. The proposed methodology has shown the capability to approximate real-world scenarios of MDOF base excitation, as evidenced by its performance when compared to Finite Element (FE) results from an actual aerospace case.

Further research could follow this work. More specifically, opportunities abound for validating the proposed approach across additional diverse case studies, including random

vibrations and fatigue evaluation when 6DOF loads are addressed to.

This research represents a step toward bridging the gap between theory and practice in the realm of mechanical load severity comparison, offering a starting point upon which future advancements can be built.

Bibliography

[1] *ECSS-E-10-03A:Testing*, 2 2002.

[2] *MIL-STD-810G : ENVIRONMENTAL ENGINEERING CONSIDERATIONS AND LABORATORY TESTS*, 10 2008.

[3] *ECSS-E-ST-20-08C: Photovoltaic assemblies and components*, 7 2012.

[4] *ECSS-E-HB-32-26A: Spacecraft mechanical loads analysis handbook*, 2 2013.

[5] *ECSS-E-HB-32-25A: Mechanical shock design and verification handbook*, 7 2015.

[6] Vega-c launcher user's manual - issue 0 revision 0, 2018. URL `https://www.arianespace.com/wp-content/uploads/2018/07/Vega-C-user-manual-Issue-0-Revision-0_20180705.pdf`.

[7] C. Amzallag, J. Gerey, J. L. Robert, and J. Bahuaud. Standardization of the rainflow counting method for fatigue analysis. *International journal of fatigue*, 16(4):287–293, 1994.

[8] R. Ayres, M. A. Underwood, and T. Keller. Controlling 6-dof systems with multiple exciters. *Sound & Vibration*, 47(10), 2013.

[9] M. A. Biot. *Transient oscillations in elastic systems*. PhD thesis, California Institute of Technology, 1932.

[10] R. R. Craig Jr and A. J. Kurdila. *Fundamentals of structural dynamics*. John Wiley & Sons, 2006.

[11] S. De Bruyne, H. Van der Auweraer, B. Peeters, J. Anthonis, M. Appolloni, and A. Cozzani. Model based control of a multi-axis hydraulic shaker using experimental modal analysis. *IFAC Proceedings Volumes*, 45(16):524–528, 2012.

[12] S. J. DiMaggio, B. H. Sako, and S. Rubin. Analysis of nonstationary vibroacoustic flight data using a damage-potential basis. *Journal of spacecraft and rockets*, 40(5): 682–689, 2003.

[13] G. J. Dodds and J. D. Robson. Road simulation. *Journal of Automotive Engineering*, 3(4):17–19, 1972.

[14] H. A. Gaberson and R. H. Chalmers. Modal velocity as a criterion of shock severity. *Shock and Vibration Bulletin*, 40(2):31–49, 1969.

[15] V. J. Grillo. Damage based analysis (dba): Theory, derivation and practical application - using both an acceleration and pseudo-velocity approach. 2016.

[16] G. R. Henderson and A. G. Piersol. Fatigue damage related descriptor for random vibration test environments. *Sound and Vibration*, 29(10):20–25, 1995.

[17] F. V. Hunt. Stress and strain limits on the attainable velocity in mechanical vibration. *The Journal of the Acoustical Society of America*, 32(9):1123–1128, 1960.

[18] T. Irvine. An introduction to the shock response spectrum. *Rev P, Vibrationdata*, 2002.

[19] T. Irvine. A fatigue damage spectrum method for comparing power spectral density base input specifications. *Revision A, Vibrationdata*, 2014.

[20] R. D. Kelly and G. Richman. *Principles and Techniques of Shock Data Analysis*, volume 5. Shock and Vibration Information Center, US Department of Defense, 1971.

[21] G. Lachenmayr. Multi-axis transient vibration testing of space objects: Test philosophy, test facility, and control strategy. In *NASA. Goddard Space Flight Center, The Seventeenth Space Simulation Conference. Terrestrial Test for Space Success*, 1992.

[22] C. Lalanne. *Mechanical vibration and shock analysis, random vibration*, volume 3. John Wiley & Sons, 2014.

[23] C. Lalanne. *Mechanical vibration and shock analysis, specification development*, volume 5. John Wiley & Sons, 2014.

[24] S. I. McNeill. Implementing the fatigue damage spectrum and fatigue damage equivalent vibration testing. In *Presented at the 79th Shock and Vibration Symposium: October*, volume 26, page 30, 2008.

[25] J. Minderhoud. Methodologies for calculating fatigue, 2011. URL `https://vibrationresearch.com/resources/methodologies-for-calculating-fatigue/`.

[26] U. Musella, G. D'Elia, A. Carrella, B. Peeters, E. Mucchi, F. Marulo, and P. Guil-

laume. A minimum drives automatic target definition procedure for multi-axis random control testing. *Mechanical Systems and Signal Processing*, 107:452–468, 2018.

[27] U. Musella, M. A. Blanco, D. Mastrodicasa, G. Monco, D. L. Emilio, M. Simone, B. Peeters, E. Mucchi, and P. Guillaume. Combining test and simulation to tackle the challenges derived from boundary conditions mismatches in environmental testing. In *Sensors and Instrumentation, Aircraft/Aerospace, Energy Harvesting & Dynamic Environments Testing, Volume 7: Proceedings of the 37th IMAC, A Conference and Exposition on Structural Dynamics 2019*, pages 259–269. Springer, 2020.

[28] B. Peeters, J. Debille, P. Sas, and B. VanHal. Multiple-input-multiple-output random vibration control: theory and practice. In *PROCEEDINGS OF ISMA 2002: INTERNATIONAL CONFERENCE ON NOISE AND VIBRATION ENGINEERING, VOLS 1-5*, pages 507–516. KATHOLIEKE UNIV LEUVEN, DEPT WERKTUIGKUNDE, 2002.

[29] D. O. Smallwood et al. An improved recursive formula for calculating shock response spectra. *Shock and vibration bulletin*, 51(2):211–217, 1981.

[30] M. A. Underwood, T. Keller, and R. Ayres. Multi-shaker control a review of the evolving state-of-the-art. *Sound and Vibration*, 51(8):8–16, 2017.

[31] J. J. Wijker. *Random vibrations in spacecraft structures design: theory and applications*, volume 165. Springer Science & Business Media, 2009.

A | Appendix A

A.1. Coefficients of the Craig's recurrence formulas

$$A = \frac{1}{\omega_n^2 \omega_d\, dt}\left\{e^{-\beta\, dt}\left[\left(\frac{\omega_d^2-\beta^2}{\omega_n^2}-\beta\, dt\right)\sin\omega_d\, dt-\left(\frac{2\omega_d\,\beta}{\omega_n^2}+\omega_d\, dt\right)\cos\omega_d\, dt\right]+\frac{2\beta\omega_d}{\omega_n^2}\right\}$$

$$B = \frac{1}{\omega_n^2 \omega_d\, dt}\left[e^{-\beta\, dt}\left(-\frac{\omega_d^2-\beta^2}{\omega_n^2}\sin\omega_d\, dt+\frac{2\omega_d\,\beta}{\omega_n^2}\cos\omega_d\, dt\right)+\omega_d\, dt-\frac{2\beta\omega_d}{\omega_n^2}\right]$$

$$C = e^{-\beta\, dt}\left(\cos\omega_d\, dt+\frac{\beta}{\omega_d}\sin\omega_d\, dt\right)$$

$$D = \frac{1}{\omega_d}e^{-\beta\, dt}\sin\omega_d\, dt$$

$$A' = \frac{1}{\omega_n^2 \omega_d\, dt}\left\{e^{-\beta\, dt}\left[\left(\beta+\omega_n^2 dt\right)\sin\omega_d\, dt+\omega_d\cos\omega_d dt\right]-\omega_d\right\}$$

$$B' = \frac{1}{\omega_n^2 \omega_d\, dt}\left[-e^{-\beta\, dt}\left(\beta\sin\omega_d\, dt+\omega_d\cos\omega_d dt\right)+\omega_d\right]$$

$$C' = -\frac{\omega_n^2}{\omega_d}e^{-\beta\, dt}\sin\omega_d\, dt$$

$$D' = e^{-\beta\, dt}\left(\cos\omega_d\, dt-\frac{\beta}{\omega_d}\sin\omega_d\, dt\right)$$

where $\beta = \xi\omega_n$.

A.2. Coefficients of the Smallwood's recursive formula

$$a_1 = -2C \quad ; \quad a_2 = E^2$$
$$b_0 = 1 - S' \quad ; \quad b_1 = 2(S' - C) \quad ; \quad b_2 = E^2 - S'$$
$$\omega_d = \omega_n \sqrt{1 - \xi^2}$$
$$E = e^{-\xi \omega_n dt} \quad ; \quad K = \omega_d \, dt \quad ; \quad C = E \cos K \quad ; \quad S = E \sin K \quad ; \quad S' = \frac{S}{K}$$

B | Appendix B

B.1. Bode gain-phase relation

The MATLAB function *invfreqs* plays a pivotal role in our analysis, and it demands access to both the magnitude and phase information of the frequency response of the shape filter to derive its coefficients. We've already established how to obtain the magnitude of the response from the APSD using Equation B.1.

$$|H_f(j\omega)| = \sqrt{APSD(\omega)} \tag{B.1}$$

However, a missing piece of the puzzle is the phase information. To bridge this gap, we employ the Bode gain-phase relation, a fundamental relationship that links the natural logarithm of the magnitude of the frequency response to the phase angle of the frequency response. This relation is expressed as follows:

$$\angle\left[H(j\omega)\right] = -\mathcal{H}\left\{\log\left(|H(j\omega)|\right)\right\} \tag{B.2}$$

Here, $\angle\left[H(j\omega)\right]$ represents the phase angle of the frequency response at a given frequency ω. The term $\mathcal{H}$ denotes the Hilbert transform, a mathematical operation that plays a pivotal role in extracting phase information from the magnitude response.

The Hilbert transform is mathematically defined as:

$$\mathcal{H}(x(t)) = \frac{1}{\pi}\int_{-\infty}^{\infty}\frac{x(\tau)}{t-\tau}\mathrm{d}\tau \tag{B.3}$$

This operation effectively extracts the phase information required to complete the frequency response characterization, enabling us to utilize the *invfreqs* function and derive the coefficients of the shape filter.

C | Appendix C

C.1. Coefficients of the pseudo velocity recursive formula

$$a_0 = 1 \quad ; \quad a_1 = -2C \quad ; \quad a_2 = E^2$$

$$b_0 = \frac{1}{T_s\omega_n^2}\left[2\xi(C-1) + \frac{(2\xi^2-1)}{\sqrt{1-\xi^2}} + T_s\omega_n\right]$$

$$b_1 = \frac{1}{T_s\omega_n^2}\left[-2CT_s + 2\xi(1-E^2) - \frac{2(2\xi^2-1)S}{\sqrt{(1-\xi^2}}\right]$$

$$b_2 = \frac{1}{T_s\omega_n^2}\left[E^2(T_s\omega_n + 2\xi) - 2\xi C - \frac{(2\xi^2-1)S}{\sqrt{1-\xi^2}}\right]$$

$$E = e^{-\xi\omega_n t} \quad ; \quad K = T_s\omega_d \quad ; \quad C = E\cos K \quad ; \quad S = E\sin K$$

$$w_d = w_n\sqrt{1-\xi^2}$$

List of Figures

List of Tables

List of Symbols

Variable	Description	SI unit
x	First displacement component in a Cartesian coordinate system	m
y	Second displacement component in a Cartesian coordinate system	m
z	Third displacement component in a Cartesian coordinate system	m
θ	First rotation component in a Cartesian coordinate system	Rad
ϕ	Second rotation component in a Cartesian coordinate system	Rad
ψ	Third rotation component in a Cartesian coordinate system	Rad
m	Mass	kg
k	Stiffness	$\frac{N}{m}$
c	Damping	$\frac{Ns}{m}$
f	Frequency	Hz
F	Force	N
M	Moment	Nm
u	Absolute displacement	m
r	Relative displacement	m
$\ddot{b}$	Enforced accelerarion	$\frac{m}{s^2}$
ω	Angular frequency	$\frac{Rad}{s}$
Q	Quality factor	-
ξ	Damping ratio	-
dt	Time step	s
t	Time	s
T	Time duration	s
$a_{sw}(t)$	Sine sweep function	-
K_e	Sine sweep rate	$\frac{oct}{min}$

Variable	Description	SI unit
$\underline{\underline{M}}$	Mass matrix	kg
$\underline{\underline{C}}$	Damping matrix	$\frac{Ns}{m}$
$\underline{\underline{K}}$	Stiffness matrix	$\frac{N}{m}$
$\underline{F}$	Force vector	N
$\underline{\underline{0}}$	Matrix of zeros	-
$\underline{\underline{I}}$	Identity matrix	-
$\underline{\bar{x}}$	State vector	$Variable$
$\underline{\bar{y}}$	State output	$Variable$
$\underline{\underline{\bar{A}}}$	State matrix	$Variable$
$\underline{\underline{\bar{B}}}$	Input matrix	$Variable$
$\underline{\underline{\bar{C}}}$	Output matrix	$Variable$
$\underline{\underline{\bar{D}}}$	Feedthrough matrix	$Variable$
$\underline{\underline{\sigma^2_{\bar{x}\bar{x}}}}$	Variance of the state	$Variable$
$\sigma^2_{\bar{y}\bar{y}}$	Variance of the output	$Variable$
W	Two-sided PSD of a white noise	$\frac{g^2}{Hz}$
W_0	One-sided PSD of a white noise	$\frac{g^2}{Hz}$
$H_f(j\omega)$	Shape filter transfer function	-
$SDOF\_TR$	Transmissibility of a SDOF system	-
$SDOF\_PV\_TR$	Pseudo velocity transmissibility of a SDOF system	-
$SDOF\_RD\_TR$	Relative displacement transmissibility of a SDOF system	-
α	Slope of the S-N curve	-
S	Stress	MPa
D	Fatigue damage	-
c	Constant of proportionality	-
σ_{pv}	Pseudo velocity root mean square	
g_i	Coordinates of the center of mass with respect to the base IF	m
I_{ij}	Moments of inertia of the structure with respect to the base IF	kgm^2
$\underline{\underline{R}}$	Eigenvectors matrix	-
$\underline{k}_{guess}$	Initial guess for the diagonal terms of the stiffness matrix	$Variable$
$\underline{f}$	Vector of the first six natural frequencies	Hz

List of Acronyms

2DOF 2 Degree of Freedom.
3DOF 3 Degree of Freedom.
6DOF 6 Degree of Freedom.

AA Absolute Acceleration.
APSD Acceleration Power Spectral Density.

CLA Coupled Load Analysis.

ECSS European Cooperation for Space Standardization.
ERS Extreme Response Spectrum.
ESI Equivalent Sine Input

FDET Fatigue Damage Equivalent Testing.
FDS Fatigue Damage Spectrum.
FE Finite Element.
FEMAP Finite Element Modeling And Postprocessing.
FOS Factor of Safety.
FRA Frequency Response Analysis.

IF Interface
IUT Item Under Test.

LV Launch Vehicle.
LVUM Launch Vehicle User's Manual

MDOF Multi Degree of Freedom.
MIL-STD Military Standard.
MIMO Multiple-Input and Multiple-Output.

NASTRAN NAsa STRucture ANalysis.

PSD Power Spectral Density.
PV Pseudo Velocity.

QSL Quasi-Static Load

RBM Rigid Body Motion.
RD Relative Displacement.
RMS Root Mean Square.

SC Spacecraft.
SDOF Single Degree of Freedom.
SRS Shock Response Spectrum.

TS Telescope.

Acknowledgements

I extend my sincere gratitude to my advisor, Professor Lorenzo Dozio, the coordinator of the aerospace engineering program at Politecnico di Milano. His unwavering support and the invaluable opportunity to undertake this thesis in collaboration with Thales Alenia Space have been instrumental in shaping my academic and professional development.

I am equally thankful to my co-advisor, Dr. Pietro Nali, whose guidance, assistance, and insightful suggestions have greatly enriched my thesis work. Dr. Nali is not only a knowledgeable and experienced mentor but also a kind and helpful person. His talent for inspiring curiosity and passion, fueling interest and enthusiasm, has been a profound influence on my educational journey. I have learned a tremendous amount from him, and his mentorship has been invaluable in my academic endeavors.

I also wish to express my heartfelt appreciation to my family and all those who have supported me throughout my academic years at Politecnico di Milano. Your unwavering support and encouragement have been indispensable in helping me reach this significant milestone in my academic and professional journey.